RESEARCH ARTICLE

Key Points:
- Forty-one new campaign GPS velocities from the San Bernardino Mountains and vicinity
- San Jacinto Fault slipping faster than San Andreas Fault
- Geodetic and geologic rates for ECSZ agree except near 1992 and 1999 earthquakes

Kinematic modeling of fault slip rates using new geodetic velocities from a transect across the Pacific-North America plate boundary through the San Bernardino Mountains, California

Sally F. McGill[1], Joshua C. Spinler[2], John D. McGill[3], Richard A. Bennett[2], Michael A. Floyd[4], Joan E. Fryxell[1], and Gareth J. Funning[5]

[1]Department of Geological Sciences, California State University, San Bernardino, San Bernardino, California, USA, [2]Department of Geosciences, University of Arizona, Tucson, Arizona, USA, [3]Department of Physics, California State University, San Bernardino, San Bernardino, California, USA, [4]Department of Earth, Atmospheric and Planetary Sciences, Massachusetts Institute of Technology, Cambridge, Massachusetts, USA, [5]Department of Earth Sciences, University of California, Riverside, California, USA

Abstract Campaign GPS data collected from 2002 to 2014 result in 41 new site velocities from the San Bernardino Mountains and vicinity. We combined these velocities with 93 continuous GPS velocities and 216 published velocities to obtain a velocity profile across the Pacific-North America plate boundary through the San Bernardino Mountains. We modeled the plate boundary-parallel, horizontal deformation with 5–14 parallel and one obliquely oriented screw dislocations within an elastic half-space. Our rate for the San Bernardino strand of the San Andreas Fault (6.5 ± 3.6 mm/yr) is consistent with recently published latest Quaternary rates at the 95% confidence level and is slower than our rate for the San Jacinto Fault (14.1 ± 2.9 mm/yr). Our modeled rate for all faults of the Eastern California Shear Zone (ECSZ) combined (15.7 ± 2.9 mm/yr) is faster than the summed latest Quaternary rates for these faults, even when an estimate of permanent, off-fault deformation is included. The rate discrepancy is concentrated on faults near the 1992 Landers and 1999 Hector Mine earthquakes; the geodetic and geologic rates agree within uncertainties for other faults within the ECSZ. Coupled with the observation that postearthquake deformation is faster than the pre-1992 deformation, this suggests that the ECSZ geodetic-geologic rate discrepancy is directly related to the timing and location of these earthquakes and is likely the result of viscoelastic deformation in the mantle that varies over the timescale of an earthquake cycle, rather than a redistribution of plate boundary slip at a timescale of multiple earthquake cycles or longer.

1. Introduction

The ~330 km wide transform plate boundary between the Pacific and North American Plates in Southern California comprises a complex system dominated by northwest striking, right-lateral faults, accompanied locally by east striking thrust, reverse, and left-lateral faults (Figure 1). The total rate of relative motion between these plates in Southern California is 52 ± 2 mm/yr [*DeMets and Dixon*, 1999], but geologic, geodetic, and seismologic communities have not agreed about how this strain is partitioned among the various faults of the southern San Andreas system.

The Eastern California Shear Zone (ECSZ) was recognized as an important element of this plate boundary as early as 1990 [*Dokka and Travis*, 1990; *Savage et al.*, 1990]—a role confirmed by two recent surface-rupturing earthquakes: the 1992 *M*7.3 Landers earthquake and the 1999 *M*7.1 Hector Mine earthquake (Figure 1). Present-day strain rates determined from GPS and other geodetic techniques imply higher fault slip rates in this region [*Sauber et al.*, 1994; *Savage et al.*, 2001; *Meade and Hager*, 2005; *Spinler et al.*, 2010] than indicated from geologic studies [*Oskin et al.*, 2007, 2008].

The relative role of the San Andreas and San Jacinto Faults also remains a topic of ongoing investigation (see summary in *McGill et al.* [2013]). Bedrock offsets along the San Andreas Fault [e.g., *Powell*, 1993] are an order of magnitude larger than for the (younger) San Jacinto Fault [*Sharp*, 1967; *Matti and Morton*, 1993], but the relative significance of the two faults in terms of present-day activity and seismic hazard may be more equal. South of San Gorgonio Pass (Figure 1), most geodetic studies suggest an equal or slightly larger role for the San Andreas Fault (16–26 mm/yr) than for the San Jacinto Fault (9–21 mm/yr) [*Bennett et al.*, 1996;
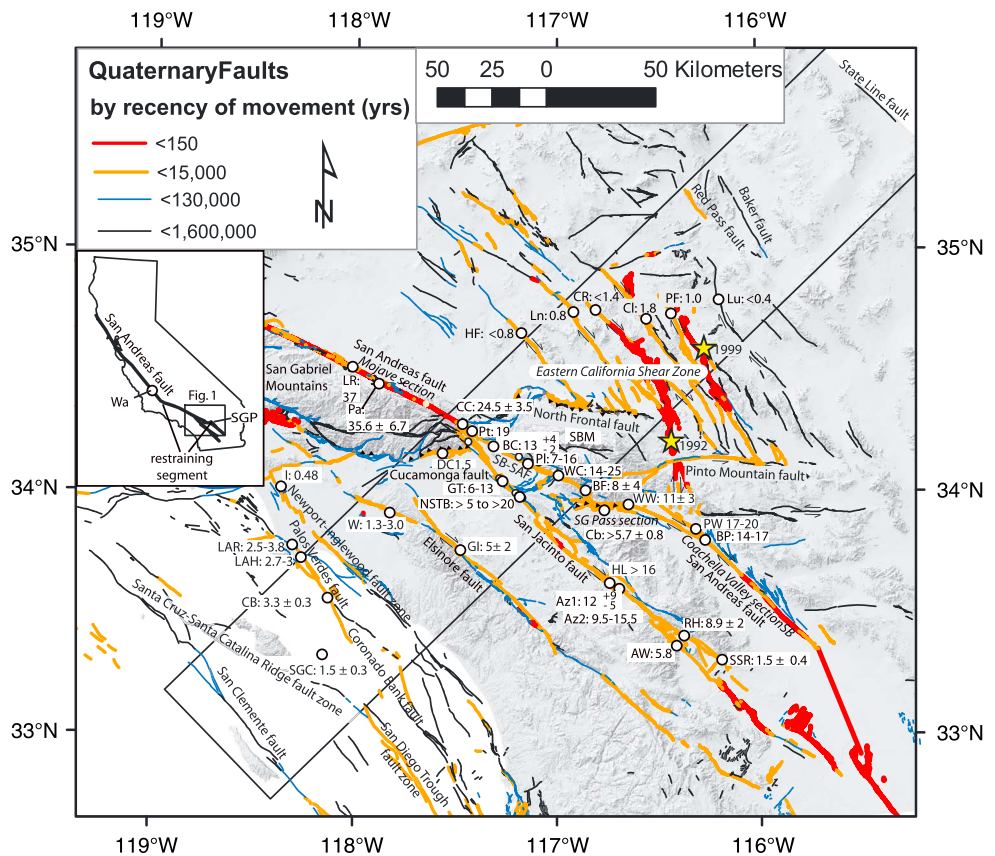
Figure 1. Location of modeled area, within northeast oriented black rectangle. Faults are from the *U.S. Geological Survey and California Geological Survey* [2006]. White circles show locations of late Quaternary geologic slip rate estimates, with rates given in mm/yr. Inset map of California shows location of Figure 1. AW, Ash Wash [*Blisniuk et al.*, 2011]; Az1, Anza [*Rockwell et al.*, 1990]; Az2, Anza [*Blisniuk et al.*, 2013]; BC, Badger Canyon [*McGill et al.*, 2010]; BF, Burro Flats [*Orozco*, 2004; *Orozco and Yule*, 2003; *Yule and Spotila*, 2010; see also *Yule*, 2009]; BP, Biskra Palms [*Behr et al.*, 2010; *Fletcher et al.*, 2010; see also *van der Woerd et al.*, 2006; *Keller et al.*, 1982]; Cb, Cabezon [*Yule et al.*, 2001]; CB, Coronado Bank [*Brankman and Shaw*, 2009]; CC, Cajon Creek [*Weldon and Sieh*, 1985]; Cl, Calico fault [*Oskin et al.*, 2007]; CR, Camp Rock fault [*Oskin et al.*, 2008]; DC, Day Canyon [*Horner et al.*, 2007]; GT, Grand Terrace [*Prentice et al.*, 1986]; GI, Glen Ivy [*Millman and Rockwell*, 1986]; HF, Helendale fault [*Oskin et al.*, 2008]; I, Inglewood oil field, [*Freeman et al.*, 1992]; LAH, Los Angeles Harbor [*McNeilan et al.*, 1996]; LAR, Los Angeles River [*Stephenson et al.*, 1995]; Ln, Lenwood fault [*Oskin et al.*, 2008]; LR, Littlerock [*Weldon et al.*, 2008; *Matmon et al.*, 2005]; Lu, Ludlow fault [*Oskin et al.*, 2008]; NSTB, Northern San Timoteo badlands [*McGill et al.*, 2012; *Onderdonk et al.*, 2015; *Kendrick et al.*, 2002]; Pa, Pallett Creek [*Salyards et al.*, 1992]; PF, Pisgah fault [*Oskin et al.*, 2008]; Pl, Plunge Creek [*McGill et al.*, 2013]; Pt, Pitman Canyon [*McGill et al.*, 2010]; RH, Rockhouse Canyon [*Blisniuk et al.*, 2010]; SBM, San Bernardino Mountains; SB-SAF, San Bernardino strand San Andreas Fault; SGC, San Gabriel Channel [*Ryan et al.*, 2012]; SG Pass (and SGP, in inset), San Gorgonio Pass; SSR, southern Santa Rosa Mountains [*Blisniuk et al.*, 2010]; W, Whittier fault [*Rockwell et al.*, 1992]; Wa, Wallace Creek [*Sieh and Jahns*, 1984]; and WC, Wilson Creek [*Harden and Matti*, 1989]. The Long Canyon, Burnt Mountain, and Eureka Peak faults are not labeled but are the three faults that extend southward from the 1992 epicenter toward the Coachella section of the San Andreas Fault.

Becker et al., 2005; *Fay and Humphreys*, 2005; *Meade and Hager*, 2005; *Fialko*, 2006; *Spinler et al.*, 2010; *Loveless and Meade*, 2011; *Lindsey and Fialko*, 2013], although one study using a viscoelastic rheology infers greater slip on the San Jacinto Fault (24–26 mm/yr) than on the San Andreas Fault (16–18 mm/yr) [*Lundgren et al.*, 2009].

In contrast, elastic models constrained by geodetic data generally suggest a much reduced role for the San Andreas Fault in the San Bernardino Valley and San Gorgonio Pass [*Becker et al.*, 2005; *Meade and Hager*, 2005; *Spinler et al.*, 2010]. In these models, a substantial portion of the inferred slip rate across the Coachella Valley section of the San Andreas Fault passes northward to the ECSZ (13.5–18 mm/yr according to *Spinler et al.* [2010]), rather than remaining on the San Andreas Fault. Likewise, a substantial portion of the inferred slip rate across the Mojave section of the San Andreas Fault appears, in these models, to extend southward onto the San Jacinto Fault, leaving a very low inferred slip rate on the San Bernardino section of the San Andreas

Fault (e.g., 5.1 ± 1.5 mm/yr [*Meade and Hager*, 2005], −2.3 ± 15 mm/yr (best fitting rate had left-lateral slip, but with large uncertainty) [*Becker et al.*, 2005], 5–8 mm/yr [*Spinler et al.*, 2010], and 8.2–10.5 mm/yr [*Loveless and Meade*, 2011]). *Chuang and Johnson* [2011] estimated a rate of 8.2 ± 1.9 mm/yr using a viscoelastic model constrained by both geodetic data and geologic slip rates. One study that suggests a higher slip rate across this part of the San Andreas Fault (14.3 mm/yr) [*McCaffrey*, 2005] does so only as a result of including geologic slip rate data in the same inversion with the geodetic data, using rates of 18–30 mm/yr for this section of the fault, which no longer represent the best geologic estimates [see *McGill et al.*, 2013].

These low rates of present-day elastic strain accumulation across the San Bernardino and San Gorgonio Pass sections of the San Andreas Fault contrasted dramatically with Holocene and late Pleistocene slip rate estimates published in the 1980s (24.5 ± 3.5 mm/yr at Cajon Creek [*Weldon and Sieh*, 1985] and 14–25 mm/yr at Wilson Creek [*Harden and Matti*, 1989]; see Figure 1 for locations.), which are 3–5 times faster than rates inferred from modeling of geodetic data. Recent work, however, has shown that the slip rate for the past 10–35 kyr is lower than previously thought, only 7–16 mm/yr at Plunge Creek [*McGill et al.*, 2013] and a similar rate (~11–17 mm/yr) at Badger Canyon [*McGill et al.*, 2010]. The higher rate at Cajon Creek (24.5 ± 3.5 mm/yr [*Weldon and Sieh*, 1985]) can be explained by slip transfer from the northern end of the San Jacinto Fault onto the San Andreas Fault [*McGill et al.*, 2013]. The rate at Wilson Creek (14–25 mm/yr [*Harden and Matti*, 1989]) is based on an age estimate from the degree of soil profile development rather than from direct dating. It consequently has a large uncertainty that is not inconsistent with the newly published rate at Plunge Creek [*McGill et al.*, 2013].

The new San Andreas Fault slip rate estimates at Plunge Creek and Badger Canyon [*McGill et al.*, 2010, 2013] overlap with the rates inferred from geodesy alone by *Loveless and Meade* [2011] and marginally with *Spinler et al.* [2010] and *Meade and Hager* [2005], but not with *Becker et al.* [2005]. Although any potentially remaining discrepancy is not large, we note that all of these prior estimates inferred from geodesy were based on data sets with very limited geodetic data from the San Bernardino Mountains. Our study rectifies that situation by adding velocity measurements at 22 new sites and substantially improving velocity estimates at 19 sites in and around the San Bernardino Mountains. We first present the new site velocities and then combine the new velocities with other available velocities to conduct one-dimensional elastic modeling for fault slip rates (modified to account for one obliquely oriented fault) along a 90 km wide, 520 km long transect across the plate boundary passing through the San Bernardino Mountains (Figure 1).

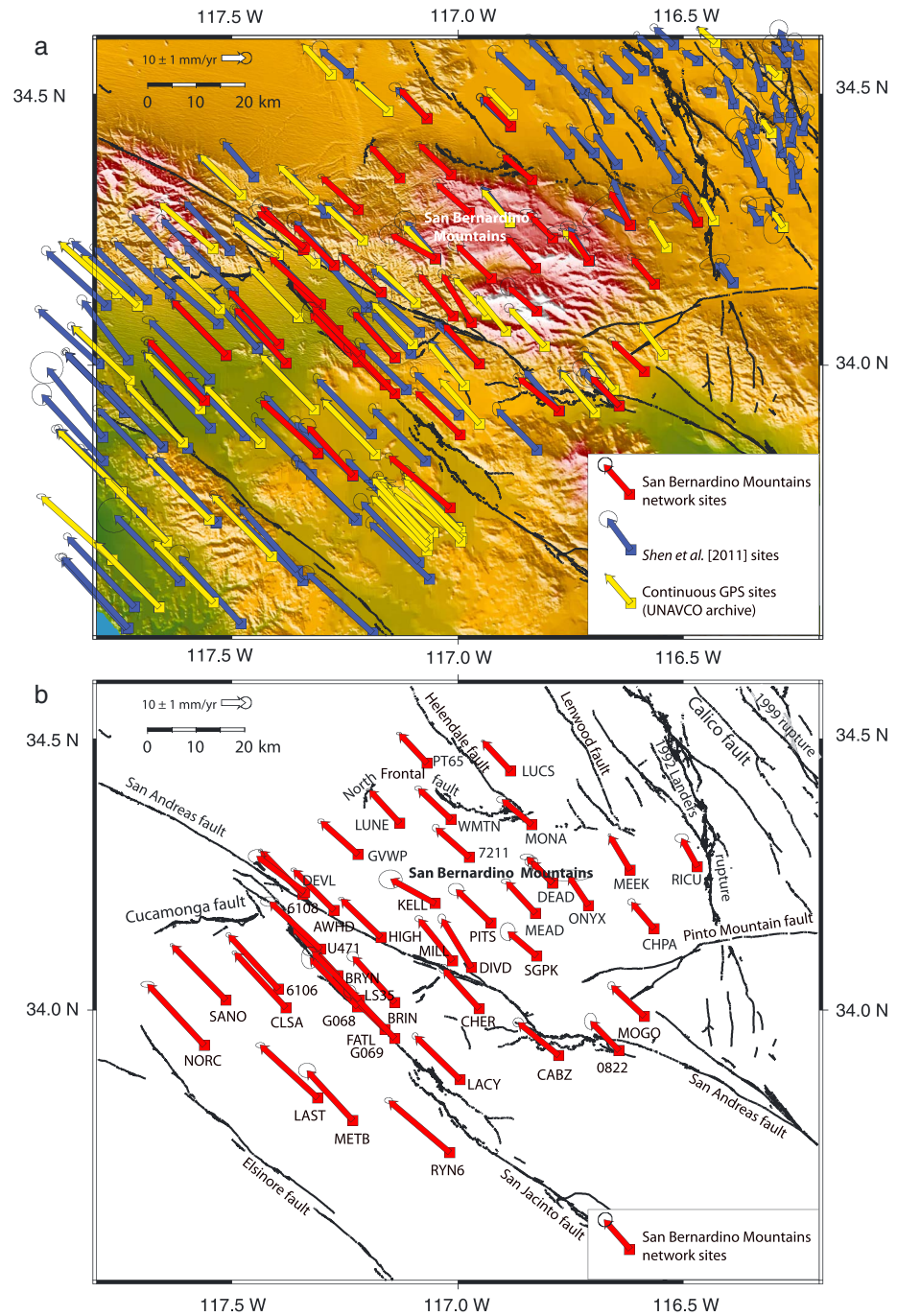## 2. New GPS Site Velocities for the San Bernardino Mountains and Vicinity

2.1. Site Velocity Methods

2.1.1. Field Observations

To improve our understanding of the crustal deformation field in the vicinity of the San Andreas and San Jacinto Faults near their juncture, we conducted repeated campaign-style GPS surveys of (mostly) existing geodetic benchmarks in the San Bernardino Mountains and in the valley areas to the southwest from 2002 to 2014 (Figure 2). We began with a set of 12 sites, along the northwestern edge of the present network (NORC, SANO, CLSA, 6106, BRYN, U471, HIGH, AWHD, 6108, KELL, PT65, and LUCS). These 12 sites were surveyed by students and local high school teachers during five campaigns coordinated by California State University, San Bernardino (CSUSB) from 2002 to 2004, with three to five 8 h days of observation at each site per campaign. These data were included in velocity estimates of *Shen et al.* [2011]. The CSUSB group continued to survey many of these sites in 2005 and 2007–2014 while also expanding the network to include an additional 21 sites farther southeast (GVWP, LUNE, WMTN, 7211, MONA, MEEK, CHPA, ONYX, DEAD, MEAD, PITS, DIVD, MILL, DEVL, CHER, CABZ, MOGO, RYN6, FATL, BRIN, and LAST). For most of these sites we collected GPS observations for three to five 24 h days per year.

We also report here new velocities for sites in this vicinity observed primarily by the University of California Riverside group (LS35) or University of Arizona group (SGPK), as well as sites observed primarily by other agencies but to which members of our groups have contributed data. This includes sites for which velocities were published by *Shen et al.* [2011] (METB, TOM2, and RICU), as well as two sites first surveyed in 2005 by the U.S. Geological Survey and the Ohio State University for the B4 lidar project (G068 and G069).

For most of the sites that we occupied, we acquired GPS carrier phase data using Ashtech ZXtreme and ZXII receivers with Ashtech choke ring antennas as well as with Topcon GB-1000 and Trimble R7 and NetR9 receivers with Zephyr geodetic antennas. For a few sites, phase data were collected with TurboRogue receivers and Dorne-Margolin choke ring antennas. Antennas were mounted on tripods or spike mounts over

Figure 2. (a) Velocity vectors for sites in the San Bernardino Mountains network, along with vectors for other sites in the vicinity. Velocities for continuous GPS sites were processed in the same reference frame as those for the San Bernardino Mountains network. Velocities from *Shen et al.* [2011] have been rotated into that frame. Faults that have slipped in the past 15,000 years are also shown [*U.S. Geological Survey and California Geological Survey*, 2006]. (b) Velocity vectors for sites in the San Bernardino Mountains with sites and faults named.

benchmarks that were mostly preexisting. At AWHD and GVWP we installed new monuments by setting a ~20 cm long brass pin in epoxy in a hole drilled into existing concrete.

2.1.2. Site Position Estimation

Our analysis included 1015 site days of our own GPS phase observations (mostly 8 or 24 h per day) between 2002 and 2014 supplemented with 128 phase observation days from 20 sites by nine other groups, mostly

from 1993 to 2000, archived at the Southern California Earthquake Center (http://www.data.scec.org/gps/) or at University NAVSTAR Consortium (UNAVCO) (http://facility.unavco.org/data/dai2/app/dai2.html#). These supplemental data were collected by the U.S. Geological Survey, Riverside County Flood Control, University of California, Los Angeles, University of Southern California, San Bernardino County, Ohio State University, Harvey Mudd College, the National Geodetic Survey, and the Metropolitan Water District.

We analyzed all of these campaign GPS data together with phase data from 790 continuous GPS (cGPS) stations (archived at UNAVCO http://facility.unavco.org/data/dai2/app/dai2.html#), with 613 stations located throughout the deforming western U.S., 72 stations located throughout the North American Plate interior, and 103 stations distributed globally. This distribution of cGPS stations outside of the deforming plate boundary zone enabled us to effectively transform between global and North American Plate-fixed reference frames. Of these sites, 93 cGPS and 41 campaign sites are located within our study transect across the Pacific-North America plate boundary (Figure 1).

We analyzed all data following standard methods using the GAMIT/GLOBK software version 10.4 [*Herring et al.*, 2010a, 2010b], which incorporates the International GNSS Service (IGS) IGS05 absolute phase center model and the FES2004 ocean loading model. We used IGS final products for orbital parameters and IERS Bulletin B for Earth orientation parameters as a priori constraints obtained from the MIT GAMIT ftp site (ftp://chandler.mit.edu), but we estimated corrections to these a priori values. The daily position uncertainties were estimated assuming an empirical elevation angle-dependent error model based on postfit phase residuals calculated in the GAMIT module AUTCLN [*Herring et al.*, 2010a].

2.1.3. Preparation of Coordinate Time Series

We used GLOBK to obtain coordinate time series for the campaign and continuous data relative to a North America-fixed reference frame ("NA12," as defined relative to ITRF2008 by *Blewitt et al.* [2013]), using loosely constrained a priori coordinate estimates and Earth orientation parameters. We used GGMATLAB [*Herring*, 2003] to visually examine the coordinate time series data over the entire time period available (maximum range was 1993–2014) for each campaign and cGPS site in our study transect across the Pacific-North America plate boundary (Figure 1). We estimated a secular rate for each site removing individual daily position estimates that fell outside the 3 sigma confidence interval. For campaign sites, we also omitted daily position estimates for other visually detected outliers in cases where (1) individual observation log sheets noted a problem with the equipment setup (e.g., antenna substantially off level or not centered at end of day) or (2) a short observation period (e.g., only a few hours) led to a large uncertainty in the position estimate. For cGPS sites we also used GGMATLAB to estimate and remove annual and semiannual signals from the time series. The velocity uncertainties for continuous sites were determined assuming a first-order Gauss-Markov error model [e.g., *Reilinger et al.*, 2006] fit to the scatter of the postfit time series data using the "real sigma" option in the GGMATLAB module TSVIEW [*Herring*, 2003]. For the campaign sites, the observations are too temporally sparse to allow estimation of annual or semiannual signals from the time series or to use a Gauss-Markov noise model, but seasonal signals are probably averaged out over the longer histories (up to 20 years) for many of these sites [*Blewitt and Lavallee*, 2002]. Velocity uncertainty estimates for campaign sites were estimated in GGMATLAB using standard least squares error propagation methods. Weighted and normalized root-mean-square residuals are listed in Table 1 for each San Bernardino Mountains network time series and in Table S1 in the supporting information for each cGPS time series. The average weighted root-mean-square (WRMS) residuals are 4.5 mm for the campaign time series and 3.6 for the cGPS time series.

2.1.4. Earthquake Effects

Three major earthquakes occurred during or shortly prior to the time of the observations included in our analysis. The 28 June 1992 M7.3 Landers earthquake occurred less than 2 years prior to the earliest observations available at some of the campaign sites in the San Bernardino Mountains network and at three of the cGPS sites (CRPF, LBCH, and TRAK). To avoid contaminating our interseismic velocity estimates with postseismic deformation following the Landers earthquake, observations within 2.5 years after this earthquake were excluded from the velocity estimates for these sites, following the lead of *Shen et al.* [2011] and also consistent with our own observations of nonlinear trends in the time series for cGPS stations in operation at that time.

The 16 October 1999 M7.1 Hector Mine earthquake affected the entire area covered by the San Bernardino Mountains network, causing (mostly) northeast directed coseismic steps for cGPS stations in the region with amplitudes ranging from 5 mm in the southwestern part of the San Bernardino Mountains network to 150 mm near the northeastern edge. We thus allowed for a coseismic step at this time for all sites. To avoid

Table 1. Velocities for Campaign Sites in the San Bernardino Mountains Network

| Site | Longitude (deg) | Latitude (deg) | East Component | | | | North Component | | | | Number of Observations | Number of Epochs | Subtransect |
			Velocity (mm/yr)	Uncertainty (mm/yr)	WRMS (mm)	NRMS	Velocity (mm/yr)	Uncertainty (mm/yr)	WRMS (mm)	NRMS			
0822	−116.6420	33.9249	−11.9	1.01	3.44	0.52	12.22	1.39	4.77	0.83	8	4	8
6106	−117.3962	34.0383	−20.78	0.43	4.8	0.9	22.52	0.4	4.4	0.88	31	9	3
6108	−117.3420	34.2124	−17.7	0.34	4.9	1.19	18.22	0.31	4.6	1.37	27	7	2
7211	−116.9738	34.2808	−13.93	0.6	3.8	0.77	12.27	0.63	4	1.03	22	5	3
AWHD	−117.2732	34.1835	−16.8	0.48	5.8	0.95	16.86	0.3	3.7	0.61	32	9	2
BRIN	−117.1392	34.0138	−17.44	0.95	3.9	0.71	19.13	0.85	3.4	0.77	20	8	5
BRYN	−117.2656	34.0632	−18.6	0.35	4.6	0.65	20.09	0.36	4.8	0.65	39	10	3
CABZ	−116.7755	33.9159	−16.91	0.87	5.1	0.7	13.75	0.79	4.5	0.65	26	8	8
CHER	−116.9518	34.0028	−14.89	0.71	4.7	0.84	16.52	0.79	5.3	1.06	27	9	6
CHPA	−116.5641	34.1499	−9.52	0.64	4.03	0.84	11.09	0.56	3.5	0.94	33	7	7
CLSA	−117.3804	34.0036	−21.27	0.4	4.25	0.86	22.95	0.34	3.66	0.79	34	9	3
DEAD	−116.7895	34.2338	−8.76	1.12	7.5	1.22	8.91	0.85	5.7	1.04	24	7	5
DEVL	−117.3389	34.2171	−19.9	1.41	4.9	0.97	14.87	1.12	3.9	1.04	12	4	5
DIVD	−116.9692	34.0780	−12.29	0.67	5.3	1.17	20.31	0.8	6.4	1.76	31	8	5
FATL	−117.1607	33.9637	−20.46	0.75	4.8	0.89	20.08	0.67	4.2	0.9	26	9	4
G068	−117.2210	34.0051	−19.89	1.44	6.4	1.12	20.56	1.86	7.5	1.6	14	6	4
G069	−117.1388	33.9472	−18.69	1.04	4.3	0.7	19.58	1.07	4.5	0.91	17	4	2
GVWP	−117.2200	34.2862	−15.47	0.56	4.7	0.88	13.85	0.4	3.3	0.78	30	5	3
HIGH	−117.1693	34.1339	−16.52	0.47	5.4	1.14	15.97	0.27	3.1	0.75	39	9	4
KELL	−117.0495	34.1959	−18.54	1.97	9.2	1.12	10.09	1.57	7.2	0.83	16	5	4
LACY	−116.9945	33.8712	−18.62	0.49	3.5	0.66	18.14	0.57	4.2	0.98	31	5	7
LAST	−117.3092	33.8374	−23.91	0.77	5.1	1	21.95	0.44	2.9	0.67	24	5	5
LS35	−117.2168	34.0182	−19.72	1.57	7.1	1.14	20.18	0.77	3.5	0.61	12	5	3
LUCS	−116.8820	34.4395	−11.61	0.25	2.4	0.56	12.46	0.19	1.9	0.5	24	8	2
LUNE	−117.1281	34.3440	−12.58	0.55	3.3	0.76	13.69	0.26	1.6	0.46	27	6	4
MEAD	−116.8278	34.1782	−12.22	0.79	5.1	0.8	13.24	0.4	2.6	0.45	28	7	5
MEEK	−116.6174	34.2579	−8.56	0.24	3.1	0.68	14.36	0.27	3.5	0.97	43	10	6
METB	−117.2317	33.7964	−19.06	1.45	5.4	0.85	20.7	1.22	4.6	0.85	16	5	6
MILL	−117.0106	34.0907	−14.11	0.66	3.4	0.75	17.48	0.51	2.6	0.69	26	6	5
MOGO	−116.5862	33.9880	−13.71	0.61	4	0.78	12.81	0.65	4.4	1.01	30	7	8
MONA	−116.8357	34.3409	−12.33	0.91	6.4	1.38	10.51	0.59	4.1	1.12	22	6	4
NORC	−117.5610	33.9344	−23.58	1.11	5	1.23	25.41	0.51	2.2	0.64	21	6	2
ONYX	−116.7095	34.1926	−8.33	3.67	12.6	1.88	12.41	0.94	3.7	0.68	7	4	6
PITS	−116.9260	34.1605	−14.53	1.31	6.7	1.4	13.94	1.02	5.2	1.29	22	7	5
PT65	−117.0679	34.4538	−11.55	0.43	5.6	1.11	12.35	0.22	2.9	0.64	35	12	2
RICU	−116.4689	34.2641	−6.54	1.14	6.6	1.52	11.77	0.77	4.2	1.2	10	4	7
RYN6	−117.0168	33.7366	−25.49	0.68	4.3	0.78	21.64	0.48	3.1	0.71	24	5	8
SANO	−117.5131	34.0182	−22.36	0.33	3.7	0.77	22.8	0.27	3	0.72	38	12	2
SGPK	−116.8250	34.0992	−11.97	1.28	3.6	0.93	10.19	1.5	4.3	1.32	11	3	6
U471	−117.3034	34.1122	−21.12	1.56	5.9	1.12	19.72	0.82	3.1	0.61	18	6	3
WMTN	−116.5285	34.1048	−13.61	0.61	4.8	1.02	12.86	0.37	2.9	0.77	27	6	3

contaminating our interseismic velocity estimates with data influenced by postseismic deformation, we also excluded observations from any site in the study region collected during a 2.2 year period following the Hector Mine earthquake (again, following the lead of *Shen et al.* [2011] and consistent with our own observations of nonlinear trends in the time series for cGPS stations). The pre-earthquake and post-2001 velocities were constrained to be identical.

The 4 April 2010 *M*7.2 El Mayor-Cucapah earthquake affected the southern half of the San Bernardino Mountains network, creating southwest oriented displacements of 1–3 mm for cGPS stations in the southwestern quadrant of the network and southward directed displacements of 3–5 mm in the southeastern quadrant of the network. In our velocity estimates we allowed for a coseismic step at the time of this earthquake for all stations and constrained the pre-earthquake and postearthquake velocities to be identical. Because of the small coseismic offsets within the network for this earthquake, any effects of postseismic relaxation were expected to be negligible. This was confirmed by visual inspection of the cGPS time series in GGMATLAB. For most of these sites, no postseismic signal was detected. For less than half of these stations, slight changes in velocity were

observed within about 2 years after the earthquake after detrending the time series, but for 80 of the 93 cGPS sites used in our study the velocities estimated with and without the observations from the first 2.2 years after the earthquake agreed within 2 sigma errors and 88 of the velocities agreed within 3 sigma errors. In our modeling, we used the cGPS velocities obtained with omission of 2.2 years of data following the 2010 earthquake. For the campaign sites, however, we did not exclude any observations from the period following the 2010 earthquake because in many cases this would have removed ~20% of the observations on which to base a velocity. The comparison of cGPS velocities with and without omission of data following the 2010 earthquake shows that postseismic effects of this earthquake at the location of our transect are minimal. For cGPS sites, the velocities with data omission are on average 0.1 mm/yr faster than those without data omission, but this is well within the uncertainties of our campaign site velocity estimates. Our final velocity estimates are given in Table 1 for campaign sites in the San Bernardino Mountains network and in Table S1 (in the supporting information) for the cGPS sites.

2.1.5. Incorporation of Published Velocity Estimates

In order to obtain the most robust data set for modeling fault slip rates, we also used in our modeling velocities for sites within our study transect published by *Shen et al.* [2011]. We rotated the *Shen et al.* [2011] velocity field into the same reference frame as the campaign and cGPS data that we processed ourselves by minimizing the weighted sum of squared residual velocity differences at 19 cGPS sites in common between the two solutions (see Table S1 in the supporting information for identification of the sites used to constrain this rotation). For the 19 common cGPS sites used to define the rotation parameters, the normalized root-mean-square (NRMS) and weighted root-mean-square (WRMS) residual between velocities from the solution of *Shen et al.* [2011] and our solution are 1.42 and 0.34 mm/yr, respectively, for the east velocities and 1.71 and 0.29 mm/yr, respectively, for the north velocities. (See appendix of *Spinler et al.* [2010] for the formulas used for NRMS and WRMS.) An additional 36 cGPS sites in common between the two solutions were not used to constrain the rotation parameters. For these sites the NRMS and WRMS are 2.13 and 0.71 mm/yr, respectively, for the east velocities and 2.88 and 0.80 mm/yr, respectively, for the north velocities. Table S2 (in the supporting information) reports the velocities for the 216 sites from *Shen et al.* [2011] rotated into our realization of the NA12 reference frame.

2.2. Site Velocity Results

We report 41 new velocities from the vicinity of San Bernardino Mountains and valley areas to the southwest (Table 1). Figure 2 shows the velocity vectors in map view, and Figure 3 shows the time series for these sites. Of these sites, 19 had a velocity estimate in *Shen et al.* [2011] which is here updated with up to 10 years of new observations. The remaining 22 sites have velocities that are published here for the first time.

With the exception of site KELL (see Text S1 for discussion of this site), the interseismic velocities for the San Bernardino Mountains network show a smoothly varying field with all velocities oriented northwestward and with steadily increasing velocity magnitudes for sites farther and farther southwestward across the plate boundary (red arrows in Figure 2). Throughout most of the network, the horizontal velocity vectors are oriented parallel to each other (N44°W on average), but in the eastern corner of the network sites MEEK and RICU are moving in a more northerly direction (N30°W), perhaps as a result of a more northerly trending subsurface shear zone connecting the San Andreas Fault to the ECSZ [e.g., *Nur et al.*, 1993; *Rymer*, 1997; *McCaffrey*, 2005]. The velocities for the sites in the San Bernardino Mountains network are also consistent with other available velocities in the region, including the cGPS velocities (yellow arrows in Figure 2a) and campaign sites with velocities published by *Shen et al.* [2011] (blue arrows in Figure 2a).
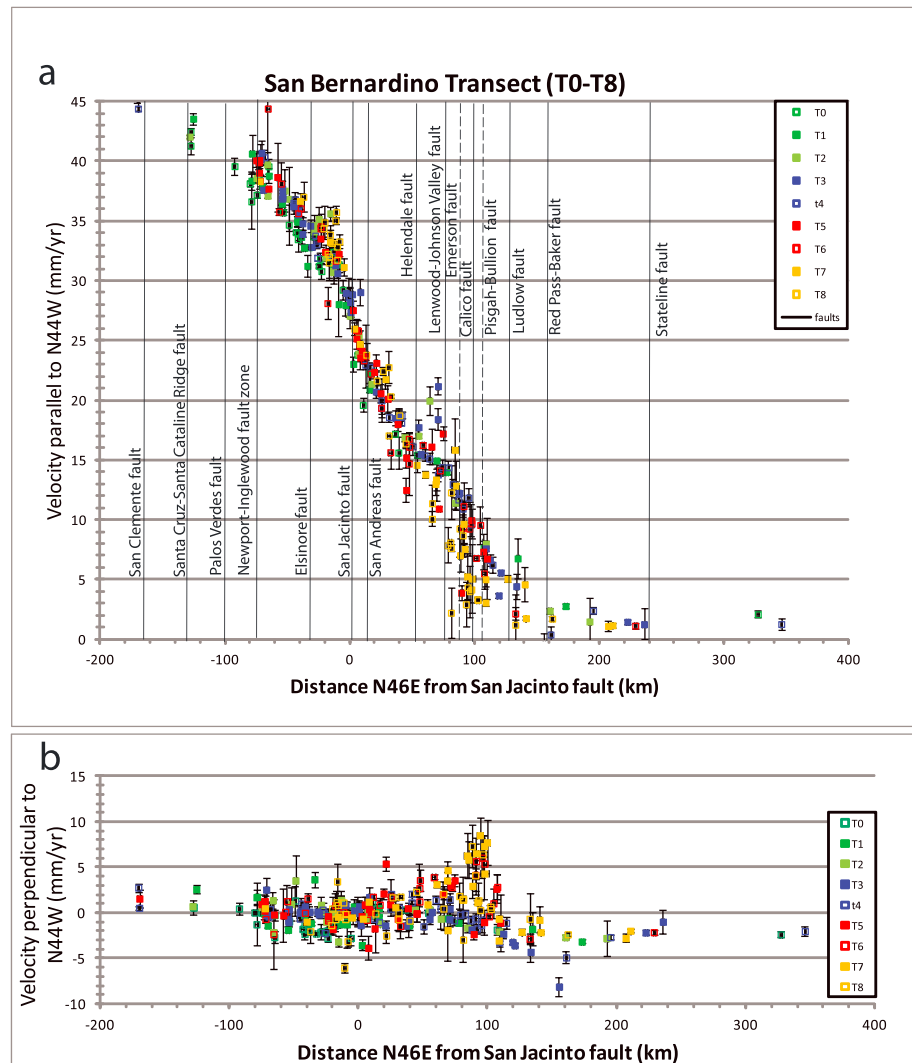
Figure 4 shows the plate boundary-parallel and -perpendicular components of velocity for the sites located within our study transect. The velocities in Figure 4 are color coded according to their location within one of nine 10 km wide subtransects (T0 to T8 in Figure 5). For our analysis, we define the orientation of the plate boundary in this region to be N44°W, which is the mean orientation of all of the site velocity vectors within the study transect and also coincides closely with the orientation of many of the mapped faults within the study transect, particularly with the San Jacinto and Elsinore Faults, both about N44.2°W within T0–T6 (Figure 5).

The two steepest sections of the velocity profile (Figure 4) are located (1) at the San Andreas and San Jacinto Faults and (2) within the ECSZ. The less steep portion of the profile in between (from about 30–80 km east of the San Jacinto Fault) suggests that there are two distinct subsurface shear zones beneath the San Andreas/San Jacinto Fault and the ECSZ, separated by a region with slower strain rate.
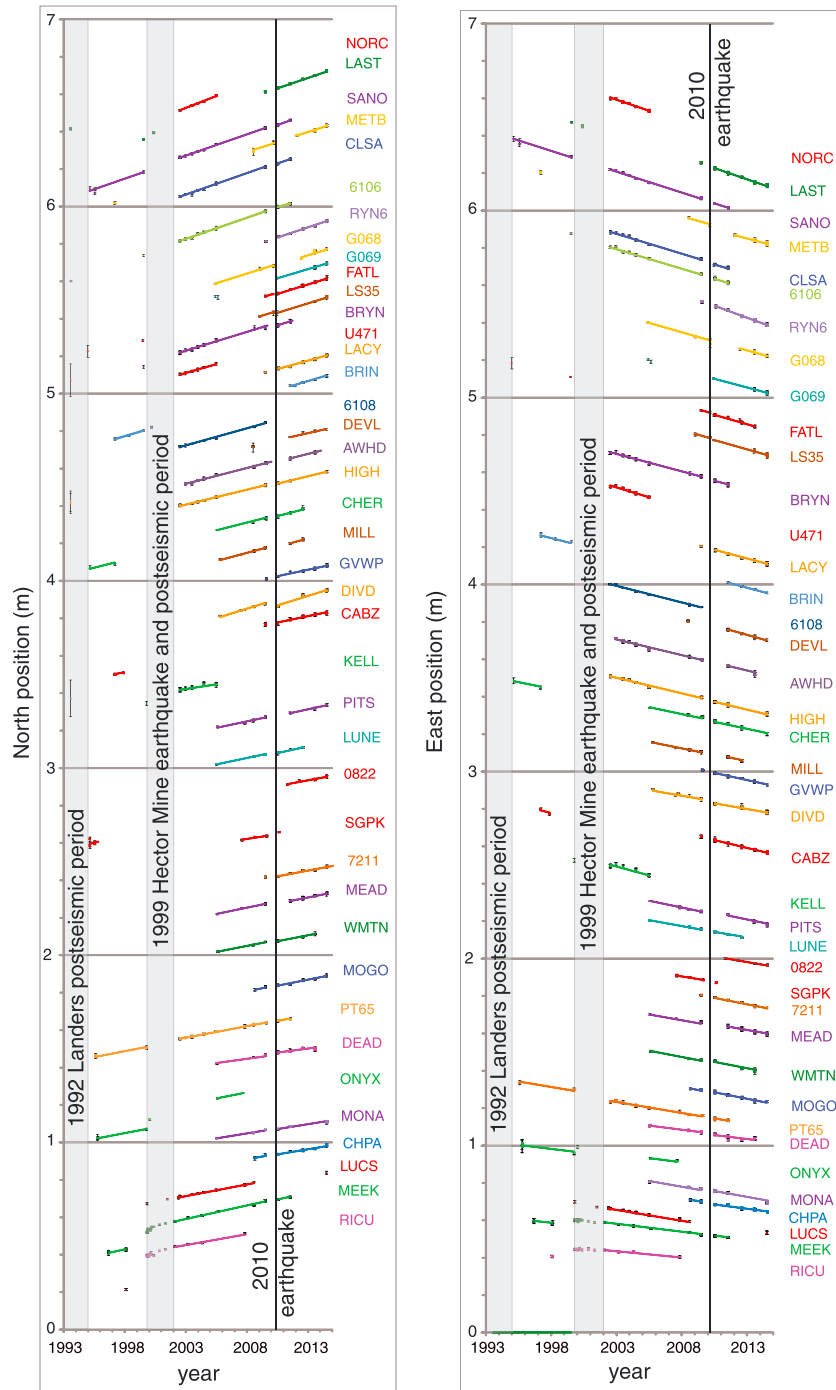
Figure 3. North and east position time series for 41 campaign GPS sites within the San Bernardino Mountains network. Absolute values of north and east position for each site have been shifted so that stations are arranged from southwesternmost (at top) to northeasternmost (at bottom). From 2002 onward, most campaigns included 3–5 days of observation at each site, although the points from adjacent days cannot be resolved individually at this scale. Coseismic steps were allowed for all sites at the times of the 1999 Hector Mine and 2010 El Mayor-Cucapah earthquakes. Vertical black lines represent the time of the 2010 El Mayor-Cucapah earthquake. Vertical gray bars show the time range from which data were considered to be influenced by postseismic deformation following the 1992 Landers and 1999 Hector Mine earthquakes. Data from this time period are plotted as points in the time series but were not used to constrain the interseismic velocities, shown by the trend lines.

Figure 4. (a) Plate boundary-parallel and (b) plate boundary-perpendicular velocities for sites within transects T0–T8 (Figure 5). Points are color coded according to the 10 km wide subtransect in which they are located (T0–T8) to show systematic changes in the velocity profile along the strike of the plate boundary. Faults marked by solid vertical lines were included in all models discussed in the text. Faults marked by dashed vertical lines (Emerson and Pisgah-Bullion faults) were included in the last model shown in Table 2.

Figure 4 shows subtle but systematic variations in the velocity profile for different subtransects, indicating changes in the deformation field along strike of the plate boundary, even over relatively short distances (a few tens of kilometers). The most obvious along-strike variation is that the steep velocity gradient in the ECSZ is located more westerly in subtransects T7 and T8 than in the subtransects located farther northwest. For subtransects T0–T6 the steepest gradient is approximately centered on the Calico fault, whereas for subtransects T7 and T8 it is centered about 10 km farther southwest along the transect (Figure 4). This may reflect that subsurface shear beneath the ECSZ is not oriented perpendicular to our transect but strikes more northerly than the plate boundary orientation, as did the 1992 Landers and 1999 Hector Mine earthquake ruptures (Figure 5). Thus, the more southeastern portion of the subsurface shear zone intersects our transect at a more southwesterly location than does the northwestern portion.

For both T0–T6 and T7 and T8, the steep velocity gradient in the ECSZ is not precisely located beneath either the 1992 or the 1999 surface ruptures but is located between them. One might have expected to see a steep velocity gradient beneath the 1992 Landers rupture in subtransects T7 and T8, as this is a likely path for
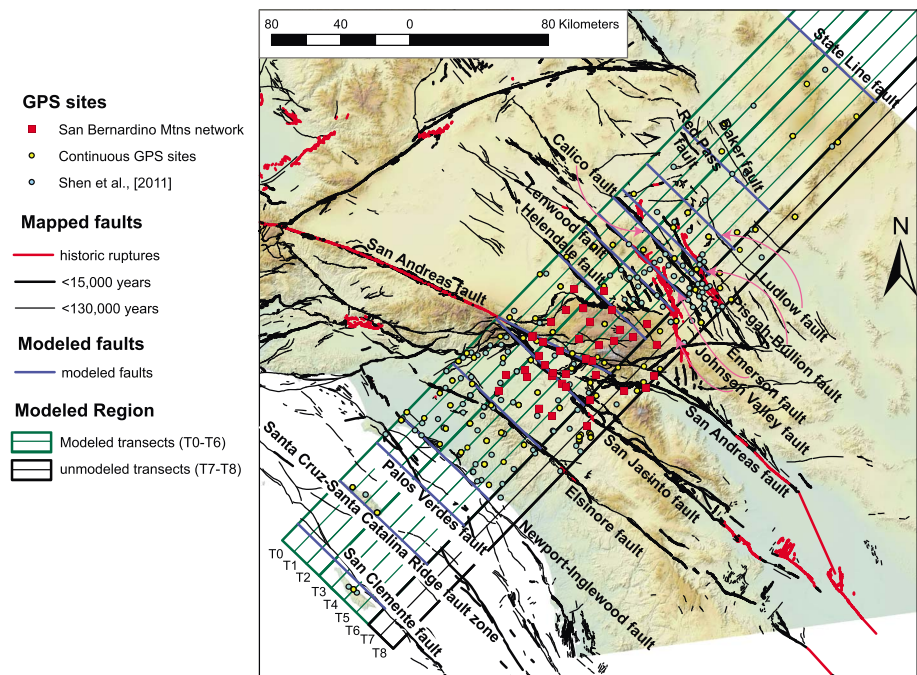
Figure 5. Location of campaign and continuous GPS sites in Southern California (small dots and squares) and the location of several 10 km wide subtransects (dark green rectangles) perpendicular to the plate boundary. Site velocities from transects T0 through T8 are plotted as a function of distance along the transect in Figure 4. Due to more complex fault geometry in transects T7 and T8, only velocities from transects T0 through T6 were included in the modeling (Figure 6).

transfer of subsurface shear from the southern San Andreas Fault into the ECSZ. Surprisingly, however, at this location (about 65–70 km northeast of the San Jacinto Fault in T7 and T8; Figure 5) the velocity profile is more gently sloping (Figure 4).

The fault geometry in subtransects T7 and T8 is more complex and cannot be modeled well with a set of parallel, dextral faults. For this reason we focus our modeling on transects T0–T6 only, where the effects of complex fault geometry are minimal (Figures 4a and 5). As shown in Figure 6, omitting data from subtransects T7 and T8 significantly reduces the scatter in the northeastern half of the velocity profile (compare to Figure 4a).

A more subtle along-strike variation in the velocity profile can be seen between the San Jacinto Fault and the coastline (0 to −100 km in Figure 4). Along this section of the profile, the velocities are progressively higher for the more southeasterly transects at any given distance along the profile. In this case, there is not just a distinctly different profile for T7 and T8 versus T0–T6 but rather a progressive change across all of the profiles. To assess the significance of this along-strike variation, we modeled subtransects T0–T2 (30 km wide) and T3–T6 (40 km wide) separately, in addition to modeling T0–T6 together (70 km wide).

Figure 6 also identifies outliers in the T0–T6 velocity profile that we removed prior to modeling. Twelve of these are from *Shen et al.* [2011]. Most of these velocities are based on limited observations, and 10 of these sites are located near the 1992 Landers and/or 1999 Hector Mine earthquake rupture. Their anomalous velocities may reflect unmodeled or incompletely modeled postseismic effects of these earthquakes. We also removed four outliers from our own San Bernardino Mountains network (DEAD, METB, ONYX, and SGPK) and one from the set of cGPS sites (LDES). Each outlier removed is discussed in Text S1.

Figure 6 displays velocities for sites from our San Bernardino Mountains network with larger symbols (see legend) to highlight the contribution of our campaign velocities toward defining the shape of the profile. In our modeling of subtransects T0–T6 we used 66 cGPS sites, 97 sites from *Shen et al.* [2011], and 29 campaign sites from the San Bernardino Mountains network.
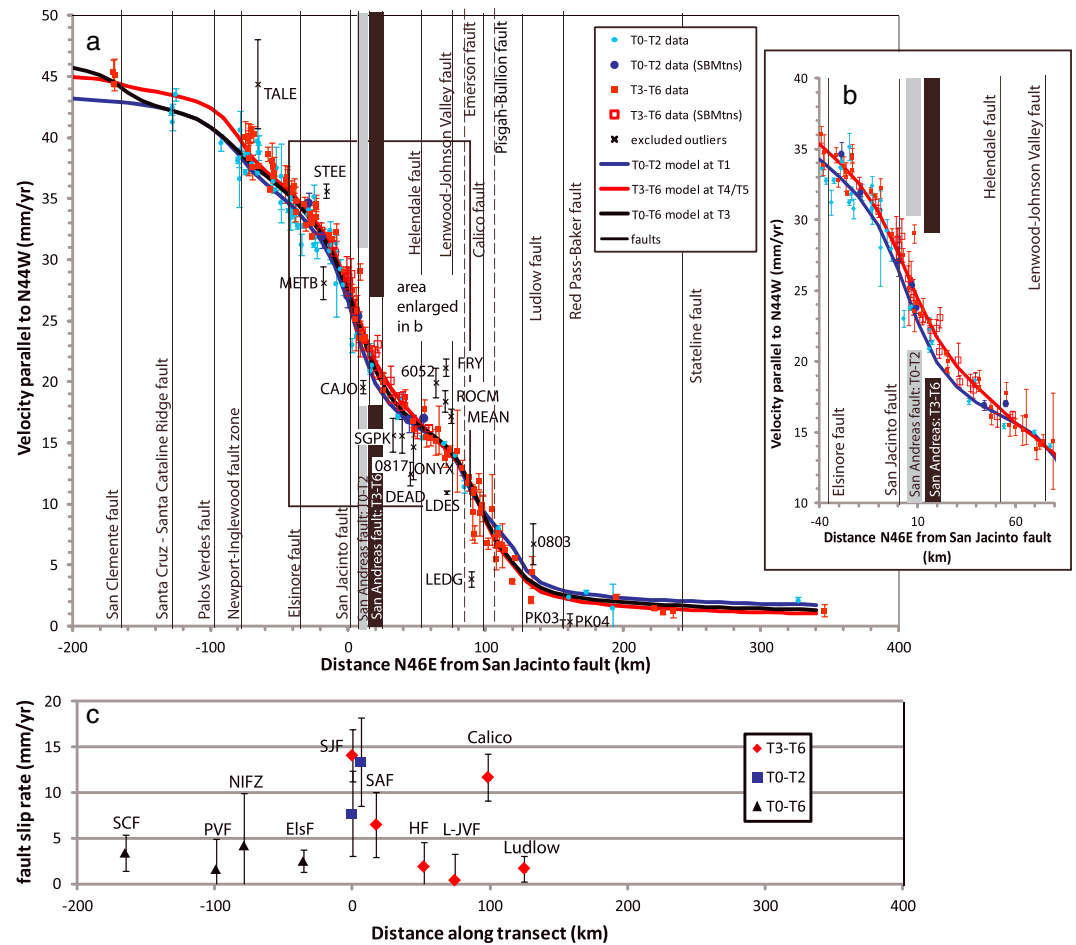
Figure 6. (a) Predicted velocity profiles when data from T0–T2 (blue) and T3–T6 (red) are modeled separately from each other and when data from T0–T6 are modeled together (black curve). Slip rates and locking depths used in these models are listed in Table 2. In all models shown in this figure, locking depths were fixed at the 95th percentile of earthquake hypocentral depths along the transect (see Figure 7). Predicted velocity profile for T0–T2 is plotted using a San Andreas Fault contribution taken from the location of the fault in the middle of T1. Predicted velocity profile for T3–T6 is plotted using a San Andreas Fault contribution taken from the location of the fault on the boundary of T4 and T5. In both cases, the fault slip rates used to generate the predicted velocity profiles are from least squares solutions in which the actual distance between each site velocity and the closest point on the San Andreas Fault were used (Table 2). Also shown are 17 outliers in the velocity profile that were excluded from the modeling. Site names for the outliers are labeled. (b) Enlargement of area near the San Andreas and San Jacinto Faults, showing evidence for different slip rates in the two transects. Velocities for campaign sites in the San Bernardino Mountains network are distinguished with different symbols (SBMtns) to show the contribution of our campaign data to constraining the models in the vicinity of the San Andreas and San Jacinto faults. (c) Modeled slip rates and 95% confidence intervals compared to geologic slip rates. Modeled slip rates plotted for faults west of the San Jacinto Fault are taken from the model for T0–T6 combined (Table 2) so as to include the largest set of site velocities to constrain the slip rates for the offshore and nearshore faults. Slip rates for faults east of the San Andreas are taken from the model for subtransects T3–T6 (Table 2) because the fault geometry in subtransects T0–T2 is more complex than can be modeled with parallel, northwest striking, right-lateral faults. The slip rates for the San Jacinto and San Andreas Faults are plotted using results from both T0–T2 and T3–T6 to show the change in rates for these two faults between these two set of subtransects. For fault abbreviations in Figure 6c, see full names for the faults located immediately above in Figure 6a.

3. Fault Slip Estimation

3.1. Elastic Modeling

In this paper we present the results of one-dimensional modeling of buried screw dislocations in an elastic half-space. Our model begins with a set of 12 parallel, N44°W striking, vertically dipping, buried screw dislocations coinciding as closely as possible with the surface traces of the right-lateral strike-slip faults that make up the

plate boundary in this region and one screw dislocation oriented N61.6°W representing the San Bernardino strand of the San Andreas Fault (Figure 5). Because the San Andreas Fault is a major component of the plate boundary system and because its obliquity is so pronounced, we made two corrections for its obliquity as described in a later paragraph.

This model (with modeled faults shown by blue lines in Figure 5) approximates the geometry of the mapped faults within subtransects T0–T6 reasonably well, with two notable exceptions. (1) Our model does not include the North Frontal thrust fault, along the northern margin of the San Bernardino Mountains, or the Cucamonga thrust fault, along the southern flank of the San Gabriel Mountains (Figure 1). Both faults are thought to have a relatively low slip rate (<1.6 mm/yr dip-slip rate for the North Frontal fault (calculated by *McGill et al.* [2013], from data presented by *May et al.* [1982], *Sadler and Trent* [1990], and *Spotila and Sieh* [2000; see also *Yule and Spotila* [2010]) and 1.9±0.5 mm/yr dip-slip rate for the Cucamonga fault [*Horner et al.*, 2007]), so their omission is not likely to have a large effect on the modeled velocities of other faults. (2) Within the ECSZ, we begin by modeling individual faults only when they are spaced more ~10 km apart. The Lenwood, Emerson, Calico, Pisgah, and Bullion faults are closely spaced within a ~32 km wide span. Of these we model only the Lenwood and Calico faults. In the models we present first, any slip on the Emerson, Pisgah, and Bullion faults is thus included in our modeled slip rates for the Lenwood and Calico faults. The Calico fault is located approximately at the center of the steepest gradient in the part of the velocity profile in the ECSZ (Figure 4). We present later the results of models in which the Emerson and Pisgah-Bullion faults were also included.

In our models, we calculate the N44°W component of the predicted velocity, v_i, of any site on the surface by summing the contributions of each of the model faults, using the following equation:

$$v_i = v_o + \Sigma_j \left(r_j/\pi\right) \cos\left(g_j\right) \tan^{-1}\left(x_{ij}/d_j\right), \tag{1}$$

(modified from *Savage and Burford* [1973] and *Okada* [1985]), where r_j is the modeled slip rate on the jth fault; g_j is the angle between the jth model fault and the reference plate boundary orientation of N44°W; x_{ij} is the distance between the ith GPS station and the jth fault, measured perpendicular to the jth fault; d_j is the locking depth of the jth fault; and v_o is a reference velocity added to translate the model from a reference frame centered on the local fault system into the reference frame of the observed velocities, centered in stable North America. We used $g_j = 0$ for all model faults except the San Andreas Fault, for which we used $g_j = -17.6°$ to compute the contribution of our N61.6°W oriented model San Andreas Fault to the N44°W oriented component of the predicted site velocities. We also accounted for the obliquity of the San Andreas Fault to the N44°W reference plate boundary by populating the appropriate column of the x_{ij} matrix with the distance between each station and the oblique (N61.6°W) model San Andreas Fault.

The equation we use for modeling assumes that the modeled faults extend infinitely along strike, which is obviously not the case here. The San Andreas Fault changes strike southeast of our transect; the Elsinore Fault terminates at and the San Jacinto Fault converges with the San Andreas Fault near the northwestern edge of our transect; most of the Eastern California Shear Zone (ECSZ) faults terminate southeast of our transect; the Ludlow fault does not extend northwestward of subtransect T3; and the Red Pass and Baker faults do not extend southeastward into subtransects T3–T6. Nonetheless, for our final, preferred model of subtransects T3–T6, most of the modeled faults extend with roughly constant strike for at least ½ transect width or more beyond both sides of the modeled regions, thus reducing the effects of finite fault lengths on our results. Within the ECSZ, the effect of finite fault lengths is also ameliorated by the fact that the Calico fault turns out to be the only ECSZ fault that plays a statistically significant role in fitting GPS site velocities (see section 3.2). Our approach also does not allow us to consider block rotations, but elastic block modeling of the northern Mojave Desert suggests that only the northeasternmost portion of our transect (east of the Calico fault) is likely to be affected by rotation [*Spinler et al.*, 2013].

In our modeling, we constrained all slip rates to be positive (right lateral). Omitting this constraint produces models with marginally smaller χ^2 values, but the left-lateral slip rates assigned to some faults (San Diego Trough, Lenwood, Red Pass Lake-Baker, and Stateline) produce a predicted velocity profile that has large-amplitude reversals of the velocity profile in regions with sparse data (offshore and near the northeastern end of the transect). We consider left-lateral slip rates for these faults to be unrealistic, given the dominantly right-lateral tectonic regime and documented right-lateral offsets on the Lenwood fault [*Oskin et al.*, 2008] and to be unwarranted given that the observed geodetic velocities do not visually suggest any reversals in these (or any) parts of the profile (Figure 6).
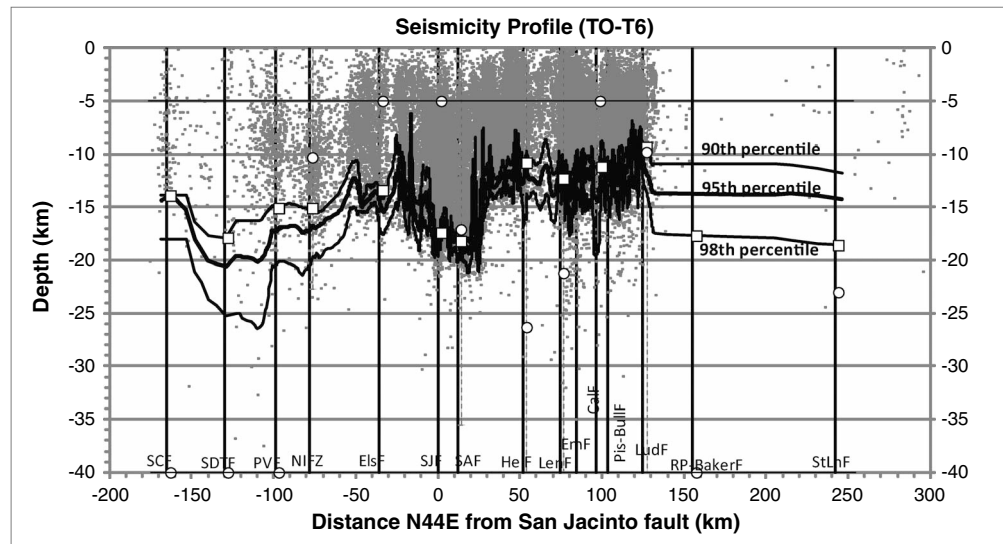
Figure 7. Cross section showing depth of seismicity along transects T0–T6, using relocated hypocenters from *Hauksson et al.* [2012]. The 90th, 95th, and 98th percentiles of hypocentral depths are also shown. The depths corresponding to each of these percentiles at each fault are listed in Tables 2 and 3. White squares and circles show the locking depths modeled by lsqcurvefit when the locking depths were constrained to be between the 90th and 98th percentiles of hypocentral depths or between 5 and 40 km depth, respectively. These symbols are shifted 2 km to the northeast from their respective faults so that the large uncertainties (gray dashed lines) can be seen. Uncertainties were not estimated for locking depths that were pushed to one of the externally applied constraints (e.g., the 90th percentile depth, 5 km, or 40 km). The values of the modeled locking depths are also given in Table 3. Vertical black lines mark locations of modeled faults.

We conducted modeling with a variety of constraints on the fault locking depths. Our preferred model uses fixed locking depths, constrained to be at the 95th percentile of earthquake hypocentral depths [*d'Alessio et al.*, 2005; *Smith-Konter et al.*, 2011]. We also tested the effect of loosening this constraint on locking depths, allowing them to vary between the 90th and 98th percentiles of hypocentral depths and to vary more widely between 5 and 40 km depth. Using hypocentral depths from *Hauksson et al.* [2012], the seismicity depth percentiles were calculated within bins of 100 earthquakes at a time (adjacent to each other along the length of the transect), with the start of each bin shifted 20 earthquakes from the previous bin. The resulting depths corresponding to a particular percentile were then smoothed by taking a running average over 20 bins (Figure 7).

To solve for slip rates with fixed locking depths, we conducted a constrained, linear least squares curve fit to the site velocities using the lsqnonneg function in MATLAB® (version R2012b). We also conducted a constrained, nonlinear least squares fit to solve for slip rates and locking depths simultaneously using the lsqcurvefit function. In both cases we minimized

$$\chi^2 = \Sigma_i (v_i - y_i)^2 s_i^{-2}, \tag{2}$$

where y_i and v_i are the observed and predicted values (respectively) of the N44°W component of the velocity of the ith site and s_i is the standard error of the N44°W component of observed velocity at the ith site. Ostensibly, 14 free parameters were solved for in the linear least squares fit including the 13 slip rates (r_j) and the reference velocity (v_o). An additional 13 parameters (the 13 locking depths (d_j)) were solved for in the nonlinear least squares fit. However, any slip rates or locking depths that were pushed to one of the constraints by the optimization routine were treated as fixed, unmodeled parameters when calculating the degrees of freedom. We used the estimate of the covariance matrix of the parameters from the curve fit to estimate the formal 95% confidence intervals for model slip rates, locking depths, and reference velocity. No uncertainties were estimated for parameters that were pushed to one of the constraints.

3.2. Modeling Results

Table 2 and Figure 6 show the best fitting models to the site velocities in T0–T2, T3–T6, and T0–T6 combined, with locking depths fixed to the 95th percentile of hypocentral depths in all three cases. For some of the modeled faults, the geometry of the actual faults is simpler in subtransects T3–T6 than in T0–T2, and our model faults coincide more closely with the actual faults there. Therefore, we base most of our analysis on the

Table 2. Comparison of Models for Various Subtransects, With Locking Depths Fixed to the 95th Percentile of Hypocentral Depths

	Model Characteristics				
Subtransects	All	T0–T6[a]	T0–T2	T3–T6[b]	T3–T6[b]
Observations	—	192	72	120	120
Modeled parameters	—	10	9	10	10
Degrees of freedom (dof)	—	182	63	110	110
χ^2	—	1115	338	586	585
χ^2/dof	—	6.12	5.36	5.33	5.31

Fault	Locking Depth Fixed 95th Percentile (km)	Modeled Slip Rate (mm/yr)	Modeled Slip Rate (mm/yr)	Modeled Slip Rate (mm/yr)	Modeled Slip Rate (mm/yr)	Late Quaternary Slip Rate (mm/yr)	References for Late Quaternary Rates
San Clemente	14.0	3.4 ± 2.0	0	1.0 ± 5.8	1.0 ± 5.8	1.8	*Field et al.* [2013]
Santa Cruz-Santa Catalina Ridge	20.6	0	0	0	0	—	None Available
Palos Verdes	17.4	1.6 ± 3.3	1.4 ± 3.6	0	0	2.5–3.6	*McNeilan et al.* [1996], *Stephenson et al.* [1995], and *Brankman and Shaw* [2009]
Newport-Inglewood	17.2	4.2 ± 3.3	5.7 ± 4.0	7.3 ± 4.8	7.3 ± 4.8	0.48	*Freeman et al.* [1992]
Elsinore	14.5	2.5 ± 1.2	2.1 ± 1.8	1.7 ± 1.7	1.7 ± 1.7	1.3–3; 4.8–7.2	*Rockwell et al.* [1992] and *Millman and Rockwell* [1986]
San Jacinto	18.1	10.8 ± 2.1	7.7 ± 4.7	14.1 ± 2.9	14.1 ± 2.9	12.5 ± 3.0	*Blisniuk et al.* [2013] and *Rockwell et al.* [1990]
San Andreas	18.1	10.4 ± 2.1	13.4 ± 4.8	6.5 ± 3.6	6.6 ± 3.5	7–16; 11–17	*McGill et al.* [2013] and *McGill et al.* [2010]
Helendale	12.7	0	0	1.9 ± 2.7	1.7 ± 2.2	<0.8 ± 0.3	*Oskin et al.* [2008]
Lenwood-Johnson Valley	11.4	1.3 ± 1.5	1.2 ± 2.6	0.4 ± 2.9	0	0.8 ± 0.2	*Oskin et al.* [2008]
Emerson	11.7	Not Modeled	Not Modeled	Not Modeled	1.3 ± 3.9	0.2–1.0	*Field et al.* [2013]
Calico	14.4	11.4 ± 2.1	9.0 ± 4.1	11.7 ± 2.6	10.8 ± 4.2	1.8 ± 0.3	*Oskin et al.* [2007]
Pisgah-Bullion	11.0	Not Modeled	Not Modeled	Not Modeled	0	1.0 ± 0.2	*Oskin et al.* [2008]
Ludlow	10.4	1.6 ± 1.1	3.6 ± 2.4	1.7 ± 1.4	1.9 ± 1.5	<0.4 ± 0.2	*Oskin et al.* [2008]
Red Pass-Baker	13.8	0	0	0	0	—	None Available
State Line	14.2	0	0	0	0	0.1–0.2	*Anderson* [1998]

[a]Preferred model for faults west of the San Jacinto Fault.
[b]Preferred models for faults including and east of the San Jacinto Fault.

results from subtransects T3–T6. For the offshore faults, however, it is more appropriate to use the results from T0 to T6 combined, because the stations on Santa Catalina Island are all located in subtransects T0–T2 while those on San Clemente Island are all located in subtransects T3–T6 (Figures 5 and 6).

Table 3 shows the effects that loosening the constraints on the locking depth have on our estimated slip rates in T3–T6. When the locking depths are allowed to vary between the 90th and 98th percentile of earthquake depths, the slip rates are very similar to those with locking depth fixed to the 95th percentile depth and the improvement in χ^2 (Table 3) is insignificant at the 5% level using an F test. Given a null hypothesis that allowing locking depths to vary between the 90th and 98th percentiles of hypocentral depths has no effect on the goodness of fit, there is a >5% chance (in fact a 22% chance) of obtaining the observed F value (1.51) if the null hypothesis is true. For most faults the optimization routine pushed the locking depths to the shallower constraint and never reached an optimal locking depth, except for the San Andreas Fault (at 18.2 km).

When locking depths were allowed to vary between 5 and 40 km, χ^2 improved significantly (Table 3), with a 20% improvement in χ^2/degrees of freedom (dof) and < 0.01% chance of obtaining the observed F value (6.33) if the null hypothesis (that allowing locking depths to vary between 5 and 40 km does not improve the fit) is true. However, the locking depths for some faults were pushed to the 5 km depth constraint, which seems physically unrealistic. In the cases where an optimal locking depth was found, the 95% confidence interval on the locking depth is extremely large (plus/minus tens to hundreds of kilometers; Table 3) and includes the locking depths used in our model with locking depths fixed at the 95th percentile of hypocentral depths. This suggests that the geodetic velocity profile is not highly sensitive to locking depth, and we thus use the models with fixed locking depths (Table 2) in our interpretations in section 4.

Table 3. Comparison of Models for Subtransects T3–T6 With Various Constraints on Locking Depth

	Model Characteristics		
Observations	120	120	120
Modeled parameters	10	11	14
Degrees of freedom (dof)	110	109	106
χ^2	586	578	473
χ^2/dof	5.33	5.30	4.46
	Preferred Model	Locking Depths Constrained Between 90th–98th Percentiles	Locking Depth Constrained Between 5–40 km

Fault	Modeled Slip Rate[a] (mm/yr)	Fixed Locking Depth at 95th Percentile (km)	Modeled Slip Rate[a] (mm/yr)	Modeled Locking Depth[a] (km)	Constraints on Locking Depth (km)	Modeled Slip Rate[a] (mm/yr)	Modeled Locking Depth[a] (km)
San Clemente	1.0 ± 5.8	14.0	0.9 ± 6.1	13.9	13.9–18.0	0	40
Santa Cruz-Santa Catalina Ridge	0	20.6	0	17.9	17.9–25.1	0	40
Palos Verdes	0	17.4	0	15.1	15.1–20.5	0	40
Newport-Inglewood	7.3 ± 4.8	17.2	7.3 ± 4.8	15.1	15.2–20.6	8.0 ± 2.8	10.3 ± 12.4
Elsinore	2.7 ± 1.7	14.5	1.9 ± 2.2	13.4	13.4–16.7	3.2 ± 1.7	5
San Jacinto	14.1 ± 2.9	18.1	13.7 ± 3.3	17.4	17.4–19.0	7.4 ± 2.1	5
San Andreas	6.5 ± 3.6	18.1	6.8 ± 7.6	18.2 ± 23.0	17.1–20.2	8.2 ± 8.7	17.1 ± 18.4
Helendale	1.9 ± 2.7	12.7	1.9 ± 2.9	10.8	10.8–16.5	6.0 ± 51.1	26.3 ± 81.8
Lenwood-Johnson Valley	0.4 ± 2.9	11.4	1.3 ± 2.9	12.3	10.9–12.3	2.8 ± 76.8	21.2 ± 445.1
Calico	11.7 ± 2.6	11.7	9.7 ± 2.3	11.2	11.2–18.3	6.2 ± 8.4	5
Ludlow	1.7 ± 1.4	14.4	2.6 ± 1.3	9.3	9.3–12.1	3.7 ± 16.4	9.8 ± 46.7
Red Pass-Baker	0	11.0	0	17.7	10.9–17.7	0	40
State Line	0	10.4	0	18.6	11.7–18.6	0	23

[a]Reported uncertainties in slip rate and locking depth are the 95% confidence intervals. Uncertainties were not calculated for cases where the slip rate or locking depth was pushed to the predefined upper or lower constraint by the optimization routine.

The better fit achieved by models with shallower locking depth (Table 3) may reflect strain localization related to an unmodeled compliant zone surrounding some of the faults [e.g., *Chen and Freymueller*, 2002; *Jolivet et al.*, 2009] rather than a shallow locking depth. In particular, a compliant zone has been recognized surrounding the Calico fault [*Barbot et al.*, 2009; *Cochran et al.*, 2009]. Including compliant zones around some faults is beyond the scope of this paper but may be worth considering in future efforts.

The 13 faults included in our primary model are not all necessary in order to achieve a good fit to the observed site velocities. For subtransects T0–T6, four of the 13 modeled faults (Santa Cruz-Santa Catalina Ridge, Helendale, Red Pass-Baker, and Stateline) are best fit with slip rates of 0 mm/yr (Table 2) and thus do not contribute to the fit. A model that also excludes the Palos Verdes fault has a nearly indistinguishable χ^2 (1118) and χ^2/dof (6.10) from the models using 13 faults ($\chi^2 = 1115$ and χ^2/dof (6.12) Table 2). Two (and only two) other modeled faults (Lenwood-Johnson Valley and Ludlow) can be removed from the model without significantly degrading the fit (using an *F* test with a 5% significance level). The resulting model with only six faults (San Clemente, Newport-Inglewood, Elsinore, San Jacinto, San Andreas, and Calico) has $\chi^2 = 1155$ and χ^2/dof = 6.24 (Table S3). Nonetheless, the following discussion focuses primarily on the models using 13 faults presented in Table 2. While the models with fewer faults fit nearly as well, the removal from the model of faults that are known to have Holocene or late Pleistocene displacement may result in artificially high modeled slip rates on the remaining faults.

4. Discussion

4.1. San Andreas and San Jacinto Faults

For subtransects T0–T6, the optimization placed about 21.2 mm/yr on the San Andreas and San Jacinto Faults combined, with slip proportioned roughly equally between the two faults (Table 2). When subtransects T0–T2 and T3–T6 are considered separately, the slip rate across these two faults combined is about the same, but the distribution of slip between the two faults appears to vary along strike. In subtransects T3–T6, the

San Andreas Fault is slipping more slowly (6.5 ± 3.6 mm/yr) than the San Jacinto Fault (14.1 ± 2.9 mm/yr). In subtransects T0–T2, where the two faults converge upon each other, the San Andreas Fault slip rate increases along strike to 13.4 ± 4.6 mm/yr and the San Jacinto Fault slip rate decreases to 7.7 ± 4.7 mm/yr (Table 2 and Figure 6c). This along-strike trend likely reflects slip transferring from the northern end of San Jacinto Fault onto the San Andreas in subtransect T1. Allowing the locking depths to vary between the 90th and 98th percentiles of hypocentral depths does not change the modeled slip rate of either fault significantly (Table 3).

Outside of the zone of slip transfer between the San Jacinto and San Andreas Faults, our preferred rate for the San Bernardino strand of the San Andreas Fault (6.5 ± 3.6 mm/yr, within subtransects T3–T6) is slightly faster than but consistent within uncertainties with the 5.1 ± 1.5 mm/yr rate estimated for this fault by *Meade and Hager* [2005] but is significantly faster than *Becker et al.*'s [2005] rate (−2.3 ± 15 mm/yr). (All reported uncertainties for our slip rate estimates are 95% confidence intervals.) Both of the previously published rates were based on elastic block modeling that used a much more limited set of geodetic velocities from the San Bernardino Mountains. Our new geodetic slip rate estimate for the San Bernardino strand in T3–T6 (with its 95% confidence interval) overlaps with the lower third of 95% confidence interval for latest Pleistocene slip rates estimated for the San Bernardino strand of the San Andreas Fault zone at Plunge Creek in subtransect T4 (7–16 mm/yr) [*McGill et al.*, 2013]. Our rate in T0–T2 (13.4 ± 4.8) is even more consistent with the rate at Badger Canyon in subtransect T2 (11–17 mm/yr) [*McGill et al.*, 2010]. (See Figure 1 for site locations.) Thus, no clear difference between the slip rate inferred from the present-day rate of strain accumulation versus from offset features of latest Pleistocene age is resolvable given the 95% confidence intervals in the estimates, although our rate estimate from geodesy for T3–T6 is on the low side of the latest Pleistocene rate estimate for that section of the fault (Figure 6c). The slightly lower rate estimated from geodesy could be the result of viscoelastic effects [*Savage and Prescott*, 1978; *Chuang and Johnson*, 2011], because this portion of the San Andreas Fault is late in its earthquake cycle. The most recent earthquake on the San Bernardino section of the San Andreas Fault is thought to have occurred over 200 years ago, in 1812 [*Seitz and Weldon*, 1994; *Yule et al.*, 2001] or earlier [*McGill et al.*, 2002], and the recurrence interval is ~150 years [*Seitz and Weldon*, 1994] to ~300 years [*Yule et al.*, 2001].

Our preferred model yields a slip rate for the San Jacinto Fault in transects T3–T6 of 14.1 ± 2.9 mm/yr, which is very similar to reported Pleistocene and Holocene rates for the San Jacinto Fault (Table 2 and Figures 1 and 6a). The best constrained geologic slip rates for the San Jacinto Fault are located southeast of our transect, at Anza, where the rate over several different timescales is 9.5–15.5 mm/yr [*Blisniuk et al.*, 2013] (see also other comparable rate estimates summarized therein). Late Pleistocene and Holocene rates for the northern San Jacinto Fault, within our transect, are more scattered, ranging from 6 to 13 mm/yr [*Prentice et al.*, 1986], 5–18 mm/yr [*McGill et al.*, 2012], and 12–19 mm/yr [*Onderdonk et al.*, 2015] to 20 mm/yr [*Morton and Matti*, 1993] or >20 mm/yr [*Kendrick et al.*, 2002]. The results of our preferred model fall well within this broad range.

The rate of present-day shear across the San Andreas and San Jacinto Faults combined (21.2 ± 2.1 mm/yr in T0–T6; Table 2) also overlaps substantially with the Holocene and latest Pleistocene slip rate of the San Andreas Fault just north of its juncture with the San Jacinto Fault (24.5 ± 3.5 mm/yr in Cajon Pass, within subtransect T0 [*Weldon and Sieh*, 1985]). Farther northwest along the San Andreas Fault, the latest Quaternary slip rate estimates summarized by *Humphreys and Weldon* [1994] are 36 ± 8 mm/yr, higher than both our estimate of the slip rate of the San Andreas and San Jacinto Faults combined and higher than published geodetic estimates of slip rate on the Mojave section of the San Andreas Fault (14.3 ± 1.2 mm/yr) [*Meade and Hager*, 2005]. The discrepancy between geologic and geodetic rates for the Mojave section of the San Andreas Fault has been explained [*Chuang and Johnson*, 2011] by the changing rates of surface deformation expected throughout the earthquake cycle for an elastic plate over a viscoelastic medium [*Savage and Prescott*, 1978]. We note, however, that even the latest Pleistocene slip rates for the San Andreas and San Jacinto Faults combined (Table 2) do not add up to the slip rate range summarized for the Mojave section of the San Andreas Fault by *Humphreys and Weldon* [1994], suggesting that either some of the rates included in the latter range may be too high or that deformation from sources other than the San Jacinto Fault and San Bernardino strand of the San Andreas Fault may be contributing to the late Pleistocene rate on the Mojave section of the San Andreas Fault, as inferred by *McGill et al.* [2013].

4.2. Eastern California Shear Zone

The Eastern California Shear Zone is not well modeled by our fault model in T0–T2. Our model extends the northwest striking, right-lateral Ludlow fault into a region where the faults mapped at the surface are

dominantly east striking and left lateral instead (Figure 5). The GPS site velocities from this region are also sparser in T0–T2 than in T3–T6. We therefore focus our discussion of the ECSZ on the results from subtransects T3–T6, where our fault model more closely approximates the actual fault geometry and where site velocities are more abundant.

4.2.1. Comparison of Our Rates With Published Geologic and Geodetic Rates

Our results from T3–T6 (Table 2) show that 15.7 ± 2.9 mm/yr of northwest oriented right-lateral shear is presently occurring in the ECSZ, comparable to ECSZ rates inferred from elastic block models (15 ± 1 mm/yr [*Meade and Hager*, 2005] and 13.5–18.0 mm/yr from four different models presented by *Spinler et al.* [2010]). As has been noted by many others, the geodetic slip rate estimates across the ECSZ are a factor of 2–3 times larger than the sum of late Pleistocene ($\leq 6.2 \pm 1.9$ mm/yr) slip rates across the zone [*Oskin et al.*, 2008].

In our models, no slip is required on the model Red Pass-Baker fault or on the model Stateline fault in order to fit the velocity profile (Table 2). These faults were included in the model because the occurrence of Holocene earthquake ruptures has been reported, both for the Red Pass fault [*U.S. Geological Survey and California Geological Survey*, 2006] and for some segments of the Stateline fault [*Anderson et al.*, 1995; *Piety*, 1995; *Menges et al.*, 2003]. *Guest et al.* [2007] report a slip rate of 2.3 ± 0.35 mm/yr for the Stateline fault since the mid-Miocene, but the late Quaternary rate is considerably slower (<0.2 mm/yr [*Anderson*, 1998]). Previously published geodetic dextral slip rates for the Stateline fault have been 0.7–1.2 mm/yr [*Hill and Blewitt*, 2006; *Guest et al.*, 2007].

Slip on the Helendale (1.9 ± 2.7 mm/yr), Lenwood (0.4 ± 2.9 mm/yr), and Ludlow (1.7 ± 1.4 mm/yr) faults is minor, agreeing, within errors, with geologic estimates for these faults of $<0.8 \pm 0.3$, 0.8 ± 0.2, and $<0.4 \pm 0.2$ mm/yr [*Oskin et al.*, 2008], respectively (Table 2 and Figure 6c). The Helendale fault is only expressed at the surface within subtransects T0–T3. In T4 it apparently terminates against the North Frontal fault. If dextral slip is indeed happening on the lower crustal root of the Helendale fault, as our preferred model weakly suggests, this would imply that the Helendale fault may continue within the footwall of the North Frontal fault, beneath the San Bernardino Mountains.

In our models, almost all of the ECSZ slip is concentrated in the vicinity of the modeled Calico fault, which is located between the 1992 Landers and 1999 Hector Mine earthquake ruptures. When the faults that ruptured in these earthquakes (the Emerson and Bullion faults) are added to the model, the uncertainties in slip rates increase, but the optimization routine still places a majority of the slip on the modeled Calico fault (10.8 ± 4.2 mm/yr), with lesser slip on the Emerson fault (1.3 ± 3.9 mm/yr) and no slip on the Pisgah-Bullion fault (Table 2). The late Pleistocene slip rate estimates (Table 2) also show the Calico fault as being the fastest of the ECSZ faults [*Oskin et al.*, 2007, 2008]. Our geodetic rate for the modeled Calico fault (10.8 ± 4.2 mm/yr), however, is a factor of 5 or more larger than the geologic estimate of 1.8 ± 0.3 mm/yr.

Thus, the large discrepancy between geodetic (15.8 ± 2.9 mm/yr) and late Pleistocene ($\leq 6.2 \pm 1.9$ mm/yr) slip rates [*Oskin et al.*, 2008] is primarily concentrated in the vicinity of the 1992 Landers and 1999 Hector Mine earthquakes. The geodetic rates for most of the other ECSZ faults agree within uncertainties with late Pleistocene rates.

4.2.2. Evaluation of the Geologic-Geodetic Rate Discrepancy

Several investigators have suggested that the lower geologic rates for the ECSZ faults may underestimate the total strain rate because they do not include permanent, off-fault deformation. Using a mechanical model of the ECSZ, *Herbert et al.* [2014] suggest that permanent, off-fault deformation accounts for $40\% \pm 23\%$ of the total strain across the ECSZ. However, this value is an average between two portions of their model area that have distinctly different behaviors. In the northern half of their model, the faults are extremely disconnected, and the estimate of off-fault deformation there is close to 60%. However, all of the late Pleistocene slip rate estimates used for comparison [*Oskin et al.*, 2007, 2008] are from the southern half of their region, where the faults are more connected and where permanent, off-fault deformation is only estimated to account for about 10% of the total strain [*Herbert et al.*, 2014].

Taking an alternate approach, *Kaneko and Fialko* [2011] and *Dolan and Haravitch* [2014] both find evidence for a deficit in surficial slip during large earthquakes from various locations around the world compared to the geodetically inferred coseismic slip at depth. *Dolan and Haravitch* [2014] compared field measurements of surficial slip in recent large earthquakes to geodetically inferred slip at depth and found that for structurally immature faults, including those that ruptured in the 1992 Landers and 1999 Hector Mine earthquakes in the ECSZ, the surface slip underestimates the slip at depth by about 40%, and they infer that the missing slip

occurs as permanent off-fault deformation. *Kaneko and Fialko* [2011] compared geodetically inferred slip at shallow depths to that at greater depth and found near-surface slip deficits of 30–60%. Using dynamic rupture simulations with elastoplastic off-fault response, they were able to account for a slip deficit of up to 15% with off-fault, plastic deformation and found that another 10% of the apparent deficit was an artifact of ignoring inelastic deformation in the geodetic inversions for coseismic slip. *McCaffrey* [2005] included inelastic deformation in his inversions of the southwestern United States and found that the western Mojave block was one of the six blocks in which inclusion of inelastic strain resulted in significant variance reduction.

It seems likely that permanent, off-fault deformation accounts for at least part of the discrepancy between slip rates estimated from offset features of late Pleistocene age (6.2 ± 1.9 mm/yr) [*Oskin et al.*, 2007, 2008] and those inferred in this paper (15.7 ± 2.9 mm/yr). Adding 40% to the total late Pleistocene rate across the ECSZ brings the total late Pleistocene rate to 8.7 ± 1.9 mm/yr. This does not overlap (at the 1σ level) with the total ESCZ rate estimated here, suggesting that other factors must be required in order to fully explain the discrepancy. Several possible explanations exist for the remaining rate discrepancy: (1) There may have been a permanent change in the distribution of lower crustal creep and/or mantle flow beneath the San Andreas Fault and the ECSZ beginning sometime in the past few thousand years and continuing indefinitely. (2) The distribution of lower crustal and mantle deformation between the ESCZ and San Andreas-San Jacinto system may fluctuate over timescales of thousands of years, in concert with earthquake clustering in the ECSZ [*Dolan et al.*, 2007; *Rockwell et al.*, 2000]. (3) The higher geodetic rates may be the result of viscoelastic flow in the mantle related to the 1992 Landers and 1999 Hector Mine earthquakes. By omitting geodetic observations from the first 2.5 and 2.2 years after the Landers and Hector Mine earthquakes, respectively, we have excluded from our velocity estimates the fast but rapidly decaying postseismic deformation that may be caused by mantle flow with a stress-dependent, power law rheology [*Pollitz et al.*, 2001; *Freed and Burgmann*, 2004; *Freed et al.*, 2006, 2007], by stress-driven creep in the lower lithosphere [*Shen et al.*, 1994; *Johnson and Segall*, 2004] and/or by poroelasticity [*Fialko*, 2004]. Nonetheless, our velocities may still reflect the longer-term process of viscoelastic mantle flow that yields deformation rates that are high after an earthquake but that decrease gradually throughout the earthquake cycle [*Savage and Prescott*, 1978].

Chuang and Johnson [2011] have demonstrated that this third mechanism can explain geologic-geodetic rate discrepancies for both the San Andreas Fault and the ECSZ. Our results (Table 2), which show that the rate discrepancy is concentrated on the Calico fault (located between the 1992 and 1999 ruptures) and (less clearly) on the Emerson fault (which ruptured in the 1992 earthquake) and that there is no rate discrepancy for other faults within the ECSZ, support this conclusion. This conclusion is also supported by the observation that after accounting for the fast, but rapidly decaying deformation in the first few years after the 1992 and 1999 earthquakes, the postearthquake deformation has converged to a stable rate (15.7 ± 2.9) that appears to be higher than the pre-1992 deformation rate of ~12 mm/yr [*Savage et al.*, 1990; *Sauber et al.*, 1994; *Savage and Svarc*, 2009].

The ~12 mm/yr, pre-1992, cumulative slip rate across the ECSZ faults may, in fact, overestimate what the deformation rate was at that time because *Sauber et al.* [1994] note that part of the strain they measured (up to 30% in the western half of the ECSZ and <10% in the eastern half) could be due to strain accumulation across the San Andreas Fault. They made no attempt to correct for this, due to uncertain modeling assumptions. Thus, it seems likely that the total rate of relative motion across faults of the ECSZ was likely significantly less than 12 mm/yr prior to 1992 and could easily have been consistent with the cumulative geologic rate that includes an estimate of off-fault deformation (8.7 ± 1.9 mm/yr, as estimated above, based on the work of *Dolan and Haravitch* [2014] and *Kaneko and Fialko* [2011]).

4.3. Faults West of the San Jacinto Fault

Slip rates for the offshore faults are not well constrained in our models due to wide spacing between the locations of site velocities. The offshore and coastal faults are best examined using subtransescts T0–T6, so as to include all of the velocity estimates from the islands (Figure 5). Our model for T0–T6 (Table 2) infers a dextral slip rate of 3.4 ± 2.0 mm/yr for the San Clemente fault, which is consistent with the 1.8 mm/yr rate used in the UCERF3 deformation model [*Field et al.*, 2013, Appendix B], which was largely based on prior geodetic results [*Bennett et al.*, 1996]. A higher rate (4–7 mm/yr) based on an offset submarine fan has been reported [*Legg*, 2005].

Our model for T0–T6 has no slip on the Santa Cruz-Santa Catalina Ridge fault (Table 2). No Quaternary rate estimates are available for this fault, but the San Diego Trough fault zone to the south (present within and south of subtransects T7–T8) has an estimated Quaternary rate of 1.5 ± 0.3 mm/yr [*Ryan et al.*, 2012]. Whether this slip on the San Diego Trough fault zone feeds into the Santa Cruz-Santa Catalina Ridge fault, the San Pedro Basin fault or the Palos Verdes fault is unclear. Our model for T0–T6 infers a small amount (1.6 ± 3.3 mm/yr) of dextral slip on the Palos Verdes fault. Several Holocene and Pleistocene slip rates are available for the Palos Verdes fault, which cluster around 3 mm/yr [*Stephenson et al.*, 1995; *McNeilan et al.*, 1996; *Brankman and Shaw*, 2009].

Our results from T0–T6 indicate that the present-day slip rate for the Newport-Inglewood fault is 4.2 ± 3.3 mm/yr. This is several times faster than the estimated geologic rate (0.48 mm/yr) [*Freeman et al.*, 1992]. Although the large uncertainty in our estimate makes the two rates potentially consistent, additional study of the Holocene or late Pleistocene slip rate of this fault would be valuable.

The Elsinore Fault splits into the Chino Hills strand and the (unmodeled) Whittier strand within subtransects T0–T2, so this fault is best examined within subtransects T3–T6. Our results for the Elsinore Fault (1.7 ± 1.7 mm/yr) are consistent with the 1.3–3.0 mm/yr Holocene slip rate for the Whittier fault [*Rockwell et al.*, 1992]. Our rate is considerably slower than late Pleistocene rates (4–7 mm/yr) obtained with age control based on soil development at Wild Rose Ranch, on the Glen Ivy segment of the fault [*Millman and Rockwell*, 1986].

5. Conclusions

Campaign GPS data collected from in and around the San Bernardino Mountains over a 12 year period (2002–2014) contribute to a refined picture of deformation across the San Jacinto and San Andreas Faults as well as the ECSZ. A transect across the Pacific-North American Plate boundary passing through the San Bernardino Mountains shows a present-day deformation profile with two prominent regions of steeper gradient. One velocity gradient is located in the vicinity of the San Andreas and San Jacinto Faults with a combined modeled slip rate of about 21 mm/yr for these two faults, representing 44% of the total deformation of about 47 mm/yr across the transect. We have imaged the transfer of slip from the northern end of San Jacinto Fault onto the San Andreas Fault with model slip rates for the San Jacinto Fault that decrease northwestward and model rates for the San Andreas Fault that increase northwestward from subtransects T3–T6 to subtransects T0–T2. The slip rate inferred for the San Jacinto Fault southeast of this region of slip transfer (14.1 ± 2.9.0 mm/yr) agrees well with published estimates for longer-term (Holocene and late Pleistocene) rates. For the San Bernardino segment of the San Andreas Fault, our geodetically estimated slip rate (6.5 ± 3.6 mm/yr outside of the region of slip transfer from the San Jacinto Fault) overlaps with the lower end of latest Pleistocene slip rate estimate on the same section of the fault. The somewhat lower geodetic estimate may be the result of viscoelastic effects on strain accumulation throughout the earthquake cycle, because the San Bernardino section of the San Andreas Fault is late in its earthquake cycle.

The other prominent velocity gradient is within the ECSZ, in the vicinity of the 1992 Landers and 1999 Hector Mine earthquakes. A combined rate of 15.7 ± 2.9 mm/yr is estimated for the model faults in ECSZ, representing 34% of the total deformation across the profile. Similar to the results of many other studies, our rates estimated from geodetic data are larger than longer-term rates estimated geologically for these faults, even when an estimate of 40% off-fault deformation is added to the geologic estimates. Our modeling of individual fault strands within the ECSZ shows that this rate discrepancy is concentrated in the vicinity of the 1992 and 1999 earthquakes and that geodetic and geologic rates agree for other parts of the ECSZ. In addition to this spatial correlation, a temporal correlation of the slip rate discrepancy with the 1992 and 1999 earthquakes is suggested by the fact that our (and others') estimates of deformation rate after these earthquakes (excluding rapid, decaying postseismic deformation) appear to be faster than the pre-1992 rate of deformation. These spatial and temporal correlations suggest that the slip rate discrepancy in the ECSZ is directly linked to these earthquakes and may be a result of viscoelastic flow in the mantle at the timescale of an earthquake cycle, rather than a longer-term redistribution of deformation between different parts of the plate boundary system.

The remaining 22% of plate boundary slip (~10 mm/yr) is distributed across several faults west of the San Jacinto Fault, with present-day deformation across the Newport-Inglewood fault occurring at a faster rate than expected from the one published geologic study available.

References

Anderson, R. E. (1998), Fault number 1076, Pahrump fault, in *Quaternary Fault and Fold Database of the United States*, U.S. Geological Survey website. [Available at http://earthquakes.usgs.gov/regional/qfaults.]

Anderson, R. E., A. J. Crone, M. N. Machette, L. A. Bradley, and S. F. Diehl (1995), Characterization of Quaternary and suspected Quaternary faults, Amargosa area, Nevada and California, *U.S. Geol. Surv. Open File Rep., 95–613*, 4 sheets, p. 44.

Barbot, S., Y. Fialko, and D. Sandwell (2009), Three-dimensional models of elastostatic deformation in heterogeneous media, with applications to the Eastern California Shear Zone, *Geophys. J. Int., 179*, 500–520.

Becker, T. W., J. L. Hardebeck, and G. Anderson (2005), Constraints on fault slip rates of the Southern California plate boundary from GPS velocity and stress inversions, *Geophys. J. Int., 160*, 634–650.

Behr, W. M., et al. (2010), Uncertainties in slip-rate estimates for the Mission Creek strand of the southern San Andreas Fault at Biskra Palms Oasis, Southern California, *Geol. Soc. Am. Bull., 122*, 1360–1377, doi:10.1130/B30020.1.

Bennett, R. A., W. Rodi, and R. E. Reilinger (1996), Global Positioning System constraints on fault slip rates in Southern California and northern Baja, Mexico, *J. Geophys. Res., 101*(B10), 21,943–21,960, doi:10.1029/96JB02488.

Blewitt, G., and D. Lavallee (2002), Effect of annual signals on geodetic velocity, *J. Geophys. Res., 107*(B7), 2145, doi:10.1029/2001JB000570.

Blewitt, G., C. Kreemer, W. C. Hammond, and J. M. Goldfarb (2013), Terrestrial reference frame NA12 for crustal deformation studies in North America, *J. Geodyn., 72*, 11–24.

Blisniuk, K., T. Rockwell, L. A. Owen, M. Oskin, C. Lippincott, M. W. Caffee, and J. Dortch (2010), Late Quaternary slip rate gradient defined using high-resolution topography and ^{10}Be dating of offset landforms on the southern San Jacinto Fault Zone, California, *J. Geophys. Res., 115*, B08401, doi:10.1029/2009JB006346.

Blisniuk, K., M. Oskin, W. Sharp, T. Rockwell, and K. Fletcher (2011), Slip rates on the southern San Jacinto Fault and Holocene-Late Pleistocene kinematics of the Pacific-North American Plate boundary, Southern California Earthquake Center Proceedings of the 2011 Annual Meeting, vol. XXI, Abstract A-152, p. 143.

Blisniuk, K., M. Oskin, A.-S. Meriaux, T. Rockwell, R. C. Finkel, and F. J. Ryerson (2013), Stable, rapid rate of slip since inception of the San Jacinto Fault, California, *Geophys. Res. Lett., 40*, 4209–4213, doi:10.1002/grl.50819.

Brankman, C., and J. H. Shaw (2009), Structural geometry and slip of the Palos Verdes fault, Southern California—Implications for earthquake hazards, *Bull. Seismol. Soc. Am., 99*, 1730–1745.

Chen, Q., and J. T. Freymueller (2002), Geodetic evidence for a near-fault compliant zone along the San Andreas Fault in the San Francisco Bay area, *Bull. Seismol. Soc. Am., 92*, 656–671.

Chuang, R. Y., and K. M. Johnson (2011), Reconciling geologic and geodetic model fault slip-rate discrepancies in Southern California: Consideration of nonsteady mantle flow and lower crustal fault creep, *Geology, 39*, 627–630.

Cochran, E. S., Y.-G. Li, P. Shearer, S. Barbot, Y. Fialko, and J. E. Vidale (2009), Seismic and geodetic evidence for extensive, long-lived fault damage zones, *Geology, 37*, 315–318.

d'Alessio, M. A., I. A. Johnson, R. Burgmann, D. A. Schmidt, and M. H. Murray (2005), Slicing up the San Francisco Bay Area: Block kinematics and fault slip rates from GPS-derived surface velocities, *J. Geophys. Res., 110*, B06403, doi:10.1029/2004JB003496.

DeMets, C., and T. H. Dixon (1999), New kinematic models for Pacific-North America motion from 3 Ma to present. I: Evidence for steady motion and biases in the Nuvel-1A model, *Geophys. Res. Lett., 26*, 1921–1924, doi:10.1029/1999GL900405.

Dokka, R. K., and C. J. Travis (1990), Role of the Eastern California Shear Zone in accommodating Pacific-North American Plate motion, *Geophys. Res. Lett., 17*, 1323–1326, doi:10.1029/GL017i009p01323.

Dolan, J. F., and B. D. Haravitch (2014), How well do surface slip measurements track slip at depth in large strike-slip earthquakes? The importance of fault structural maturity in controlling on-fault slip versus off-fault surface deformation, *Earth Planet. Sci. Lett., 388*, 38–47.

Dolan, J. F., D. D. Bowman, and C. G. Sammis (2007), Long-range and long-term fault interactions in Southern California, *Geology, 35*, 855–858.

Fay, N. P., and E. D. Humphreys (2005), Fault slip rates, effects of elastic heterogeneity on geodetic data, and the strength of the lower crust in the Salton Trough region, Southern California, *J. Geophys. Res., 110*, B09401, doi:10.1029/2004JB003548.

Fialko, Y. (2004), Evidence of fluid-filled upper crust from observations of postseismic deformation due to the 1992 M_w7.3 Landers earthquake, *J. Geophys. Res., 109*, B08401, doi:10.1029/2004JB002985.

Fialko, Y. (2006), Interseismic strain accumulation and the earthquake potential on the southern San Andreas Fault system, *Nature, 441*, 968–971, doi:10.1038/nature04797.

Field, E. H., et al. (2013), Uniform California earthquake rupture forecast, version 3 (UCERF3)—The time-independent model, *U.S. Geol. Surv. Open File Rep., 2013–1165*, p. 97, California Geological Survey Special Rep. 228, and Southern California Earthquake Center Publication 1792. [Available at http://pubs.usgs.gov/of/2013/1165/.]

Fletcher, K. E. K., W. D. Sharp, K. J. Kendrick, W. M. Behr, K. W. Hudnut, and T. C. Hanks (2010), ^{230}Th/U dating of a late Pleistocene alluvial fan along the southern San Andreas Fault, *Geol. Soc. Am. Bull., 122*, 1347–1359, doi:10.1130/B30018.1.

Freed, A. M., and R. Burgmann (2004), Evidence of power-law flow in the Mojave desert mantle, *Nature, 430*, 548–551.

Freed, A. M., R. Burgmann, E. Calais, and J. Freymueller (2006), Stress-dependent power-law flow in the upper mantle following the 2002 Denali, Alaska, earthquake, *Earth Planet. Sci. Lett., 252*, 481–489.

Freed, A. M., R. Burgmann, and T. Herring (2007), Far-reaching transient motions after Mojave earthquakes require broad mantle flow beneath strong crust, *Geophys. Res. Lett., 34*, L19302, doi:10.1029/2007GL030959.

Freeman, S. T., E. G. Heath, P. D. Guptill, and J. T. Waggoner (1992), Seismic hazard assessment-Newport-Inglewood fault zone, in *Engineering Geology Practice in Southern California, Spec. Publ.*, vol. 4, edited by B. W. Pipkin and R. J. Proctor, pp. 211–231, Assoc. of Eng. Geol., Sudbury, Mass.

Guest, B., N. Niemi, and B. Wernicke (2007), Stateline fault system: A new component of the Miocene-Quaternary Eastern California Shear Zone, *Geol. Soc. Am. Bull., 119*, 1337–1346, doi:10.1130/0016-7606(2007)119[1337:SFSANC]2.0.CO;2.

Harden, J. W., and J. C. Matti (1989), Holocene and late Pleistocene slip rates on the San Andreas Fault in Yucaipa, California, using displaced alluvial-fan deposits and soil chronology, *Geol. Soc. Am. Bull., 101*, 1107–1117.

Hauksson, E., W. Yang, and P. M. Shearer (2012), Waveform relocated earthquake catalog for Southern California (1981 to 2011), *Bull. Seismol. Soc. Am., 102*, 2239–2244, doi:10.1785/0120120010.

Herbert, J. W., M. L. Cooke, M. Oskin, and O. Difo (2014), How much can off-fault deformation contribute to the slip rate discrepancy within the Eastern California Shear Zone?, *Geology, 42*, 71–74, doi:10.1130/G34738.1.

Herring, T. A. (2003), MATLAB tools for viewing GPS velocities and time series, *GPS Solut., 7*, 194–199, doi:10.1007/s10291-003-0068-0.

Herring, T. A., R. W. King, and S. C. McClusky (2010a), GAMIT reference manual, GPS Analysis at MIT, release 10.4, Mass. Inst. Of Technol., Cambridge. [Available at http://www-gpsg.mit.edu/~simon/gtgk/GAMIT_Ref.pdf.]

Herring, T. A., R. W. King, and S. C. McClusky (2010b), GLOBK reference manual, Global Kalman filter VLBI and GPS analysis program, release 10.4, Mass. Inst. Of Technol., Cambridge. [Available at http://www-gpsg.mit.edu/~simon/gtgk/GLOBK_Ref.pdf.]

Hill, E. M., and G. Blewitt (2006), Testing for fault activity at Yucca Mountain, Nevada, using independent GPS results from the BARGEN network, Geophys. Res. Lett., 33, L14302, doi:10.1029/2006GL026140.

Horner, J. A., C. M. Rubin, and S. C. Lindvall (2007), Slip rate studies along the Sierra Madre-Cucamonga fault system using [10]Be cosmogenic and geomorphic surface age analyses, Assoc. Env. and Eng. Geol., Prog. with Abs., 50, 92.

Humphreys, E. D., and R. J. Weldon II (1994), Deformation across the western United States: A local estimate of Pacific-North America transform deformation, J. Geophys. Res., 99, 19,975–20,010, doi:10.1029/94JB00899.

Johnson, K. M., and P. Segall (2004), Viscoelastic earthquake cycle models with deep stress-driven creep along the San Andreas Fault system, J. Geophys. Res., 109, B10403, doi:10.1029/2004JB003096.

Jolivet, R., R. Burgmann, and N. Houlie (2009), Geodetic exploration of the elastic properties across and within the northern San Andreas Fault zone, Earth Planet. Sci. Lett., 288, 126–131, doi:10.1016/j.epsl.2009.09.014.

Kaneko, Y., and Y. Fialko (2011), Shallow slip deficit due to large strike-slip earthquakes in dynamic rupture simulations with elasto-plastic off-fault response, Geophys. J. Int., 186, 1389–1403, doi:10.1111/j.1365-246X.2011.05117.x.

Keller, E. A., M. S. Bonkowski, R. J. Korsch, and R. J. Shlemon (1982), Tectonic geomorphology of the San Andreas Fault zone in the southern Indio Hills, Coachella Valley, California, Geol. Soc. Am. Bull., 93, 46–56.

Kendrick, K. J., D. M. Morton, S. G. Wells, and R. W. Simpson (2002), Spatial and temporal deformation along the northern San Jacinto Fault, Southern California: Implications for slip rates, Bull. Seismol. Soc. Am., 92, 2782–2802.

Legg, M. R. (2005), Geologic slip rate on offshore San Clemente fault, Southern California, understated in GPS data, Eos Trans. AGU, 86, Fall Meet. Suppl., Abstract G53A-0876.

Lindsey, E. O., and Y. Fialko (2013), Geodetic slip rates in the southern San Andreas Fault system: Effects of elastic heterogeneity and fault geometry, J. Geophys. Res. Solid Earth, 118, 689–697, doi:10.1029/2012JB009358.

Loveless, J. P., and B. J. Meade (2011), Stress modulations on the San Andreas Fault by interseismic fault system interactions, Geology, 39, 1035–1038, doi:10.1130/G32215.1.

Lundgren, P., E. A. Hetland, Z. Liu, and E. J. Fielding (2009), Southern San Andreas-San Jacinto Fault system slip rates estimated from earthquake cycle models constrained by GPS and interferometric synthetic aperture radar observations, J. Geophys. Res., 114, B02403, doi:10.1029/2008JB005996.

Matmon, A., D. P. Schwartz, R. Finkel, S. Clemmens, and T. Hanks (2005), Dating offset fans along the Mojave section of the San Andreas Fault using cosmogenic [26]Al and [10]Be, Geol. Soc. Am. Bull., 117, 795–807, doi:10.1130/B25590.1.

Matti, J. C., and D. M. Morton (1993), Paleogeographic evolution of the San Andreas Fault in Southern California: A reconstruction based on a new cross-fault correlation, in The San Andreas Fault System: Displacement, Palinspastic Reconstruction, and Geologic Evolution, edited by R. E. Powell, R. J. Weldon, and J. C. Matti, Geol. Soc. Am. Mem., 178, 107–159.

May, S. R., C. A. Repenning, and J. D. Cooper (1982), New evidence for the age of the Old Woman Sandstone, Mojave Desert, California, J. Vertebr. Paleontol., 2(1), 109–113.

McCaffrey, R. (2005), Block kinematics of the Pacific-North America plate boundary in the southwestern United States from inversion of GPS, seismological, and geologic data, J. Geophys. Res., 110, B07401, doi:10.1029/2004JB003307.

McGill, S., et al. (2002), Paleoseismology of the San Andreas Fault at Plunge Creek, near San Bernardino, Southern California, Bull. Seismol. Soc. Am., 92, 2803–2840.

McGill, S., R. Weldon, and L. Owen (2010), Latest Pleistocene slip rates along the San Bernardino strand of the San Andreas Fault, Geol. Soc. Am. Abstr. with Prog. 42 (4) 69, paper #21-4.

McGill, S., L. Owen, E. Kent, T. Rockwell, K. Kendrick, N. Onderdonk, and E. Rhodes (2012), Slip rate of the northern San Jacinto Fault from offset landslides in the San Timoteo badlands, Seismol. Res. Lett., 83(2), 436.

McGill, S., L. Owen, R. J. Weldon, and K. Kendrick (2013), Latest Pleistocene and Holocene slip rate for the San Bernardino strand of the San Andreas Fault, Plunge Creek, Southern California: Implications for strain partitioning within the southern San Andreas Fault system for the last ~35 k.y, Geol. Soc. Am. Bull., 125(1/2), 48–72, doi:10.1130/B30647.1.

McNeilan, T. W., T. K. Rockwell, and G. S. Resnick (1996), Style and rate of Holocene slip, Palos Verdes fault, Southern California, J. Geophys. Res., 101(B4), 8317–8334, doi:10.1029/95JB02251.

Meade, B. J., and B. J. Hager (2005), Block models of crustal motion in Southern California constrained by GPS measurements, J. Geophys. Res., 110, B03403, doi:10.1029/2004JB003209.

Menges, C. M., C. Fridrich, R. J. Blakely, and R. A. Thompson (2003), Late Quaternary surface rupture and associated transpressive uplift on a section of the State Line fault in south-central Amargosa Desert Basin, southwestern Nevada, Eos Trans. AGU, 84, no. S11D-0327.

Millman, D. E., and T. K. Rockwell (1986), Neotectonics of the Elsinore Fault in Temescal Valley, California, Geol. Soc. Am. Guidebook and Volume, 82nd Annual Meeting, 82, 159–166.

Morton, D. M., and J. C. Matti (1993), Extension and contraction within an evolving divergent strike-slip fault complex: The San Andreas and San Jacinto Fault zones at their convergence in Southern California, in The San Andreas Fault System: Displacement, Palinspastic Reconstruction, and Geologic Evolution, edited by R. E. Powell, R. J. Weldon, and J. C. Matti, Geol. Soc. Am. Mem., 178, 217–230.

Nur, A., H. Ron, and G. C. Beroza (1993), The nature of the Landers-Mojave earthquake line, Science, 261(5118), 201–203.

Okada, Y. (1985), Surface deformation due to shear and tensile faults in a half-space, Bull. Seismol. Soc. Am., 75(4), 1135–1154.

Onderdonk, N., S. F. McGill, and T. K. Rockwell (2015), Short-term variations in slip rate and size of prehistoric earthquakes during the past 2000 years on the northern San Jacinto Fault Zone, a major plate boundary structure in Southern California, Lithosphere, 7, doi:10.1130/L393.1.

Orozco, A., and D. Yule (2003), Late Holocene slip rate for the San Bernardino strand of the San Andreas Fault near Banning, California, Seismol. Res. Lett., 74, 237.

Orozco, A. A. (2004), Offset of a mid-Holocene alluvial fan near Banning, CA: Constraints on the slip rate of the San Bernardino strand of the San Andreas Fault, MS thesis, 56 pp., California State Univ. at Northridge, Northridge, Calif.

Oskin, M., L. Perg, D. Blumentritt, S. Mukhopadhyay, and A. Iriondo (2007), Slip rate of the Calico fault: Implications for geologic versus geodetic rate discrepancy in the Eastern California Shear Zone, J. Geophys. Res., 112, B3042, doi:10.1029/2006JB004451.

Oskin, M., L. Perg, E. Shelef, M. Strane, E. Gurney, B. Singer, and X. Zhang (2008), Elevated shear zone loading rate during an earthquake cluster in eastern California, Geology, 36, 507–510, doi:10.1130/G24814A.

Piety, L. A. (1995), Compilation of known and suspected Quaternary faults within 100 km of Yucca Mountain, Nevada and California, U.S. Geol. Surv. Open File Rep., 94–112, 2 plates, p. 404.

Pollitz, F. F., C. Wicks, and W. Thatcher (2001), Mantle flow beneath a continental strike-slip fault: Postseismic deformation after the 1999 Hector Mine earthquake, Science, 293, 1814–1818.

Powell, R. E. (1993), Balanced palinspastic reconstruction of pre-late Cenozoic paleogeology, Southern California: Geologic and kinematic constraints on evolution of the San Andreas Fault system, in *The San Andreas Fault System: Displacement, Palinspastic Reconstruction, and Geologic Evolution*, edited by R. E. Powell, R. J. Weldon, and J. C. Matti, *Geol. Soc. Am. Mem., 178*, 1–106.

Prentice, C. S., R. J. Weldon, and K. Sieh (1986), Distribution of slip between the San Andreas and San Jacinto Faults near San Bernardino, Southern California, Geol. Soc. Am., Abstracts with Programs, 18, 172.

Reilinger, R., et al. (2006), GPS constraints on continental deformation in the Africa-Arabia-Eurasia continental collision zone and implications for the dynamics of plate interactions, *J. Geophys. Res., 111*, B05411, doi:10.1029/2005JB004051.

Rockwell, T., C. Loughman, and P. Merifield (1990), Late Quaternary rate of slip along the San Jacinto Fault Zone near Anza, Southern California, *J. Geophys. Res., 95*, 8593–8605, doi:10.1029/JB095iB06p08593.

Rockwell, T. K., E. M. Gath, and T. Gonzalez (1992), Sense and rates of slip on the Whittier fault zone, eastern Los Angeles basin, California, Association of Engineering Geologists, Annual Meeting, 35, 679.

Rockwell, T. K., S. Lindvall, M. Herzberg, D. Murbach, T. Dawson, and G. Berger (2000), Paleoseismology of the Johnson Valley, Kickapoo, and Homestead Valley faults: Clustering of earthquakes in the Eastern California Shear Zone, *Bull. Seismol. Soc. Am., 90*, 1200–1236.

Ryan, H. F., J. E. Conrad, C. K. Paull, and M. McGann (2012), Slip rate on the San Diego Trough fault zone, Inner California Borderland, and the 1986 Oceanside earthquake swarm revisited, *Bull. Seismol. Soc. Am., 102*, 2300–2312, doi:10.1785/0120110317.

Rymer, M. J. (1997), Structural link between the San Andreas Fault and the Eastern California Shear Zone, Coachella Valley and Little San Bernardino Mountains, Southern California, *Geol. Soc. Am., Abstr. Programs, 29*(5), 61–62.

Sadler, P. M., and D. D. Trent (1990), Geological transect of the central San Bernardino Mountains, Southern California, in *Guidebook, Geology of the Central San Bernardino Mountains, Southern California: Spring Meeting Guidebook, Far Western Section, National Association of Geology Teachers*, edited by D. D. Trent, pp. 36–68, Far Western Section, National Association of Geology Teachers, Glendora, Calif.

Salyards, S. L., K. E. Sieh, and J. L. Kirschvink (1992), Paleomagnetic measurements of non-brittle deformation across the San Andreas Fault at Pallett Creek, *J. Geophys. Res., 97*, 12,457–12,470, doi:10.1029/92JB00194.

Sauber, J., W. Thatcher, S. C. Solomon, and M. Lisowski (1994), Geodetic slip rate for the Eastern California Shear Zone and the recurrence time of Mojave Desert earthquakes, *Nature, 367*(6460), 264–266.

Savage, J. C., and R. O. Burford (1973), Geodetic determination of relative plate motion in central California, *J. Geophys. Res., 78*, 832–845, doi:10.1029/JB078i005p00832.

Savage, J. C., and W. H. Prescott (1978), Asthenosphere readjustment and the earthquake cycle, *J. Geophys. Res., 83*(B7), 3369–3376, doi:10.1029/JB083iB07p03369.

Savage, J. C., and J. L. Svarc (2009), Postseismic relaxation following the 1992 M7.3 Landers and 1999 M7.1 Hector Mine earthquakes, Southern California, *J. Geophys. Res., 114*, B01401, doi:10.1029/2008JB005938.

Savage, J. C., W. H. Prescott, and M. Lisowski (1990), An apparent shear zone trending north-northwest across the Mojave Desert into Owens Valley, eastern California, *Geophys. Res. Lett., 17*, 2113–2116, doi:10.1029/GL017i012p02113.

Savage, J. C., W. Gan, and J. L. Svarc (2001), Strain accumulation and rotation in the Eastern California Shear Zone, *J. Geophys. Res., 106*, 21,995–22,007, doi:10.1029/2000JB000127.

Seitz, G., and R. J. Weldon II (1994), The paleoseismology of the southern San Andreas Fault at Pitman Canyon, San Bernardino, California, in *Geological Investigations of an Active Margin*, Geol. Soc. Am., *Cordilleran Section Guidebook*, edited by S. F. McGill and T. R. Ross, pp. 152–156, San Bernardino County Museum Association, Redlands, Calif.

Sharp, R. V. (1967), San Jacinto Fault Zone in the Peninsular Ranges of Southern California, *Geol. Soc. Am. Bull., 78*, 705–730.

Shen, Z. K., D. Jackson, Y. Feng, M. Cline, M. Kim, P. Fang, and Y. Bock (1994), Postseismic deformation following the Landers earthquake, California, 28 June 1992, *Bull. Seismol. Soc. Am., 84*, 780–791.

Shen, Z.-K., R. W. King, D. C. Agnew, M. Wang, T. A. Herring, D. Dong, and P. Fang (2011), A unified analysis of crustal motion in Southern California, 1970–2004: The SCEC crustal motion map, *J. Geophys. Res., 116*, B11402, doi:10.1029/2011JB008549.

Sieh, K. E., and R. H. Jahns (1984), Holocene activity of the San Andreas Fault at Wallace Creek, California, *Geol. Soc. Am. Bull., 95*, 883–896.

Smith-Konter, B. R., D. T. Sandwell, and P. Shearer (2011), Locking depths estimated from geodesy and seismology along the San Andreas Fault system: Implications for seismic moment release, *J. Geophys. Res., 116*, B06401, doi:10.1029/2010JB008117.

Spinler, J. C., R. A. Bennett, M. L. Anderson, S. F. McGill, S. Hreinsdottir, and A. McCallister (2010), Present-day strain accumulation and slip rates associated with southern San Andreas and Eastern California Shear Zone faults, *J. Geophys. Res., 115*, B11407, doi:10.1029/2010JB007424.

Spinler, J. C., R. A. Bennett, and S. F. McGill (2013), Present-day loading rates of faults in the northern Mojave region, California, from GPS Geodesy, *Eos Trans. AGU, 95*, Abstract G41A-0907.

Spotila, J. A., and K. Sieh (2000), Architecture of transpressional thrust faulting in the San Bernardino Mountains, Southern California, from deformation of a deeply weathered surface, *Tectonics, 19*, 589–615, doi:10.1029/1999TC001150.

Stephenson, W. J., T. K. Rockwell, J. K. Odum, K. M. Shedlock, and D. A. Okaya (1995), Seismic reflection and geomorphic characterization of the onshore Palos Verdes fault zone, Los Angeles, California, *Bull. Seismol. Soc. Am., 85*, 943–950.

U.S. Geological Survey and California Geological Survey (2006), Quaternary fault and fold database for the United States, accessed 5 January 2010. [Available at USGS web site http://earthquakes.usgs.gov/regional/qfaults/.]

Weldon, R. J., II, and K. E. Sieh (1985), Holocene rate of slip and tentative recurrence interval for large earthquakes on the San Andreas Fault, Cajon Pass, Southern California, *Geol. Soc. Am. Bull., 96*, 793–81.

Weldon, R. J., K. M. Scharer, R. R. Sickler, A. H. Pruitt, C. L. Gilleland, and J. Garroway (2008), Slip rate site on the San Andreas Fault near Littlerock, California, Southern California Earthquake Center, 2008 Annual Meeting, Proceedings and Abstracts, 18, 167, Abstract #2-053.

van der Woerd, J., Y. Klinger, K. Sieh, P. Tapponnier, F. J. Ryerson, and A. Meriaux (2006), Long-term slip rate of the southern San Andreas Fault from ^{10}Be-^{26}Al surface exposure dating of an offset alluvial fan, *J. Geophys. Res., 111*, B04407, doi:10.1029/2004JB003559.

Yule, D. (2009), The enigmatic San Gorgonio Pass, *Geology, 37*, 191–192, doi:10.1130/focus022009.1.

Yule, D., and J. Spotila (2010), Quaternary geology of the San Bernardino Mountains and their tectonic margins, in *Geologic Excursions in California and Nevada: Tectonics, Stratigraphy and Hydrogeology*, edited by E. H. Clifton and R. V. Ingersoll, pp. 273–322, Pacific Section SEPM (Society for Sedimentary Geology), Upland, Calif., Book 108.

Yule, D., T. Fumal, S. McGill, and G. Seitz (2001), Active tectonics and paleoseismic record of the San Andreas Fault, Wrightwood to Indio: Working toward a forecast for the next "Big Event", in *Geologic Excursions in the California Deserts and Adjacent Transverse Ranges, Fieldtrip Guidebook and Volume*, edited by G. Dunne and J. Cooper, pp. 91–126, prepared for the Joint Meeting of the Cordilleran Section Geological Society of America and the Pacific Section American Association of Petroleum Geologists, April 9–11, 2001: Pacific Section SEPM (Society for Sedimentary Geology), Fullerton, Calif.